The Astrophysical Journal, 998:98 (17pp), 2026 February 10 https://doi.org/10.3847/1538-4357/ae2d06

SN 2024aecx: A Fast-evolving Type IIb Supernova with a Prominent Shock-cooling Peak

Qiang Xi[1,2], Ning-Chen Sun[1,2,3], David Aguado[4,5], Ismael Pérez-Fournon[4,5], Frédérick Poidevin[4,5], Junjie Jin[2], Yiming Mao[1,2], Zexi Niu[1,2], Beichuan Wang[1,2], Yu Zhang[2], Kuntal Misra[6], Divyanshu Janghel[6,7], Justyn R. Maund[8], Amit Kumar[8], Samaporn Tinyanont[9], Liang-Duan Liu[10,11,12], Yu-Hao Zhang[10,11,12], Bhavya Ailawadhi[6,13], Monalisa Dubey[6,7], Zhen Guo[14,15], Anshika Gupta[6,16], Min He[2], Dhruv Jain[6,7], Debalina Kar[6,16], Wenxiong Li[2], Joe D. Lyman[17], Haiyang Mu[1,2], Kumar Pranshu[6,18], Xinxiang Sun[1,2], Lingzhi Wang[19,20], Sarvesh Kumar Yadav[6,18], Yi-Han Zhao[1,2], Jie Zheng[2], Yinan Zhu[2], David López Fernández-Nespral[4,5], Alicia López Oramas[4,5], Yanan Wang[2], Klaas Wiersema[21], and Jifeng Liu[1,2,3]

[1] School of Astronomy and Space Science, University of Chinese Academy of Sciences, Beijing 100049, People's Republic of China; sunnc@ucas.ac.cn
[2] National Astronomical Observatories, Chinese Academy of Sciences, Beijing 100101, People's Republic of China
[3] Institute for Frontiers in Astronomy and Astrophysics, Beijing Normal University, Beijing 102206, People's Republic of China
[4] Instituto de Astrofísica de Canarias, Vía Láctea, 38205, La Laguna, Tenerife, Spain
[5] Universidad de La Laguna, Departamento de Astrofísica, 38206, La Laguna, Tenerife, Spain
[6] Aryabhatta Research Institute of Observational Sciences, Nainital—263001, India
[7] Mahatma Jyotiba Phule Rohilkhand University, Bareilly—243006, India
[8] Department of Physics, Royal Holloway, University of London, Egham, TW20 0EX, UK
[9] National Astronomical Research Institute of Thailand, 260 Moo 4, Donkaew, Maerim, Chiang Mai, 50180, Thailand
[10] Institute of Astrophysics, Central China Normal University, Wuhan 430079, People's Republic of China
[11] Education Research and Application Center, National Astronomical Data Center, Wuhan 430079, People's Republic of China
[12] Key Laboratory of Quark and Lepton Physics (Central China Normal University), Ministry of Education, Wuhan 430079, People's Republic of China
[13] Astronomy & Astrophysics Division, Physical Research Laboratory, Ahmedabad 380009, Gujarat, India
[14] Instituto de Física y Astronomía, Universidad de Valparaíso, ave. Gran Bretaña, 1111, Casilla 5030, Valparaíso, Chile
[15] Millennium Institute of Astrophysics, Nuncio Monseñor Sotero Sanz 100, Of. 104, Providencia, Santiago, Chile
[16] Department of Physics, Indian Institute of Technology Roorkee, Roorkee 247667, India
[17] Department of Physics, University of Warwick, Coventry, CV4 7AL, UK
[18] Department of Applied Optics and Photonics, University of Calcutta, Kolkata, 700106, India
[19] Chinese Academy of Sciences South America Center for Astronomy (CASSACA), National Astronomical Observatories, CAS, Beijing 100101, People's Republic of China
[20] Departamento de Astronomía, Universidad de Chile, Las Condes, 7591245 Santiago, Chile
[21] Centre for Astrophysics Research, University of Hertfordshire, Hatfield, AL10 9AB, UK
Received 2025 September 12; revised 2025 December 10; accepted 2025 December 10; published 2026 February 4

Abstract

SN 2024aecx is a nearby (∼11 Mpc) Type IIb SN discovered within ∼1 day after explosion. In this paper we report high-cadence photometric (typically 0.5 ∼ 1 day) and spectroscopic follow-up observations, conducted from as early as 0.27 day post discovery out to the nebular phase at 158.4 days. We analyze the environment of SN 2024aecx and derive a new distance (11.3 ± 1.1 Mpc), metallicity and host extinction. The light curve exhibits a hot and luminous shock-cooling peak at the first few days, followed by a main peak with very rapid postmaximum decline. The earliest spectra are blue and featureless, while from 2.3 days after discovery prominent P-Cygni profiles emerge. At nebular phase, the emission lines exhibit asymmetric and double-peaked profiles, indicating asphericity and/or early dust formation in the ejecta. Nebular spectral modelling indicates a blueshifted O-rich clump moving toward observer, and the [O I]/[Ca II] line ratio suggests an intermediate-mass progenitor. We simulated the progenitor and explosion using a two-component model of shock cooling and radioactive ^{56}Ni heating; our model favors an extended, low-mass H-rich envelope with $M_{\rm e} = 0.04 \pm 0.01\,M_{\odot}$ and a low ejecta mass of $M_{\rm ej} = 1.55^{+0.18}_{-0.14}\,M_{\odot}$. And the nebular-phase spectra and light-curve modelling both suggest that it most likely originated from an intermediate-mass binary progenitor system. The comprehensive monitoring of SN 2024aecx, coupled with the detailed characterization of its local environment, establishes it as a benchmark event for probing the progenitors and explosion mechanisms of Type IIb SNe.

Unified Astronomy Thesaurus concepts: Core-collapse supernovae (304); Galaxy distances (590); Galaxy abundances (574); Light curves (918); Spectroscopy (1558); Stellar evolution (1599)

Materials only available in the online version of record: data behind figures, machine-readable table

1. Introduction

Supernovae (SNe) are the catastrophic endpoints of stellar evolution. They inject energy, momentum, and freshly synthesized elements into the interstellar medium, thereby shaping star formation, feedback, and chemical enrichment in galaxies. Spectroscopically, SNe are divided into Type I, which lack conspicuous hydrogen Balmer features near maximum light, and Type II, which display prominent hydrogen lines (R. Minkowski 1941; A. V. Filippenko 1997). Type Ia events are the thermonuclear disruptions of carbon–oxygen white dwarfs, while the other spectral types arise from the core collapse of massive stars with initial

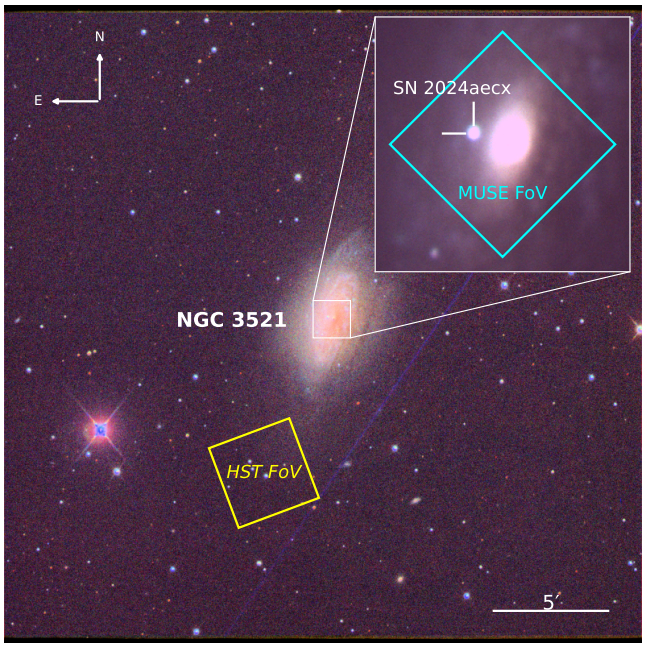

Figure 1. SN 2024aecx and its host galaxy NGC 3521. Shown is an RGB composite assembled from Las Cumbres Observatory Global Telescope network *g*-, *r*-, and *i*-band exposures; the inset at upper right highlights the enlarged region around the galaxy's nucleus, with SN 2024aecx marked by a cross. The yellow and cyan squares denote the Hubble Space Telescope/Advanced Camera for Survey and Very Large Telescope/Multi Unit Spectroscopic Explorer fields of view, respectively. North is up and East is to the left.

masses $\gtrsim$8–10 $M_{\odot}$ (A. V. Filippenko 1997; S. J. Smartt 2009). Within the core-collapse supernova (CCSN) family, Type II SNe are hydrogen-rich, Type Ib lack hydrogen but show helium, and Type Ic show neither hydrogen nor helium. The progressive loss of specific spectral features reflects different degrees of envelope stripping by line-driven winds and/or binary mass transfer of their progenitors (S. C. Yoon et al. 2010; N. Langer 2012; N. Smith 2014; Q. Fang et al. 2019; N.-C. Sun et al. 2023a). Thus, these types (Ib, Ic, and IIb) of SNe are also referred to as stripped-envelope supernovae (SESNe).

Type IIb is a transitional SN class which exhibits hydrogen lines only at early times. Within days to weeks, their hydrogen lines disappear and helium features begin to dominate (i.e., showing a Type II to Type Ib transformation) (A. V. Filippenko 1988; I. Arcavi et al. 2011). They often exhibit a short-lived, blue shock-cooling peak in their early light curves, which can sensitively constrain the progenitor radius and the mass of any residual hydrogen layer (B. P. Schmidt et al. 1993; M. Ergon et al. 2014; L. Tartaglia et al. 2017). Type IIb events are therefore powerful probes of partial envelope removal and pre-explosion mass loss.

SN 2024aecx is a nearby SN in the late-type spiral NGC 3521 (Figure 1) at a redshift of only $z = 0.002665$ and a distance of only $D = 11.3$ Mpc (see Section 3.1). It was discovered by ATLAS on 2024 December 16, 13:22:23.808 UT (MJD$_0$ = 60660.56) (H. Stevance et al. 2024). The last nondetections by ATLAS and ZTF are within ∼1 day before discovery, thereby tightly constraining the explosion epoch (I. Pérez-Fournon et al. 2024). Early follow-up spectra obtained on 2024 December 17 by the SCAT and DLT40 teams suggested a Type IIb classification, while a DLT40 spectrum on December 19 suggested a Type Ic classification (J. Andrews et al. 2024a, 2024b; J. Hinkle 2024). A comprehensive analysis by X. Zou et al. (2026)—combining dense multiband photometry with low-resolution spectroscopy—shows an early, short-lived peak arising from the shock cooling of a low-mass hydrogen envelope; their SYNAPPS spectral synthesis identifies weak H I that fades by ∼30 days after explosion, confirming the Type IIb classification.

Therefore, as a nearby Type IIb SN discovered at an exceptionally early phase and exhibiting a prominent shock-cooling peak, SN 2024aecx is a golden target for studying the progenitor and explosion physics of Type IIb SNe. Soon after discovery, we carried out rapid photometric and spectroscopic follow-up observations. Photometry was performed in both ultraviolet (UV) and optical wavelengths and the first photometric data points were acquired at only $t = 0.26$ day after discovery; we densely sampled the light curves to probe the fast evolving early peak as well as the latter evolution. We obtained the first spectrum at only $t = 0.3$ day and continued the observations through the nebular phase out to $t = 158.4$ days. In this paper, we present the results and analysis in detail.

Section 2 describes our observations of SN 2024aecx, and Section 3 analyzes its host galaxy, NGC 3521. Section 4 presents the light curves, and Section 5 shows the spectral sequence. In Section 6, we model the progenitor and bolometric light curve of SN 2024aecx. We summarize our conclusions in Section 7. All epochs in this paper are relative to discovery unless otherwise specified.

2. Observations

2.1. Photometry

2.1.1. Ground-based Telescopes

We conducted a multiband photometric monitoring campaign of SN 2024aecx in the *u*, *g*, *r*, *i*, *z* and *U*, *B*, *V*, *R*, *I* bands with six facilities: the Xinglong 60 cm telescope (H.-Y. Mu et al. 2024), the 70 cm telescope of the University of Chinese Academy of Sciences (UCAS-70; Y. Mao et al. 2025) the 1.3 m Devasthal Fast Optical Telescope (Y. C. Joshi et al. 2022), the 2.0 m Liverpool Telescope (I. A. Steele 2001), the Thai Robotic Telescope network[22] (TRT), and the Las Cumbres Observatory Global Telescope network (T. M. Brown et al. 2013). The first data points were obtained as early as $t = 0.26$ day and we used a very high cadence to densely sample the light curves. When SN 2024aecx had become substantially faint at late times, we obtained deep-field images in all observed bands with each facility to serve as template frames.

We performed image subtraction using the HOTPANTS software (A. Becker 2015) and carried out point-spread-function (PSF) photometry on the difference images with the AUTOPHOT package (S. J. Brennan & M. Fraser 2024). Photometric calibration was achieved using zero-point values derived from the template frames. For the *u*, *g*, *r*, *i*, *z* bands, we used stars from the SDSS catalog (C. P. Ahn et al. 2014) for calibration. For the *B*, *V*, *R*, and *I* bands, we calibrated against the APASS catalog (A. A. Henden et al. 2015), adopting the transformation equations of R. H. Lupton.[23] For the Johnson *U* band, we calibrated using SDSS catalog transformed via the

[22] https://trt.narit.or.th/
[23] http://www.sdss.org/dr5/algorithms/sdssUBVRITransform.html

Table 1
UV–Optical Photometry of SN 2024aecx

MJD	Instrument	Filter	Magnitude	Error
60660.56	ATLAS	*o*	14.71	0.01
60660.82	UCAS-70	*B*	14.95	0.08
60660.82	UCAS-70	*R*	14.68	0.11
60660.82	UCAS-70	*V*	14.68	0.10
60660.82	UCAS-70	*I*	14.63	0.09
60660.83	Swift/UVOT	Swift *B*	15.25	0.06
60660.83	Swift/UVOT	Swift *U*	13.98	0.05
60660.83	Swift/UVOT	UVW1	14.02	0.06
60660.84	Swift/UVOT	Swift *V*	15.14	0.08
60660.84	Swift/UVOT	UVW2	14.64	0.07

Note. Magnitudes are reported in the default photometric systems for each filter set: Johnson–Cousins UBVRI and Swift/UVOT bands are calibrated in the Vega system, whereas SDSS *ugriz*, ATLAS *c* and *o*, and the GOTO *L* band are defined in the AB system. The photometric uncertainties are given in 1σ. Only the first 10 rows are shown here; the full table is available online.

(This table is available in its entirety in machine-readable form in the online article.)

equations of S. Jester et al. (2005). A list of photometry is provided in Table 1.

2.1.2. The Swift Satellite

The UltraViolet/Optical Telescope (UVOT; P. W. A. Roming et al. 2005) onboard the Neil Gehrels Swift Observatory (N. Gehrels et al. 2004) conducted multiepoch follow-up observations of SN 2024aecx (ObsID 00018989) in the UVW2, UVM2, UVW1, *U*, *B*, and *V* filters starting from $t = 0.27$ day. Before explosion there had been archival observations of NGC 3521 in the UVW2, UVM2, and UVW1 filters (ObsID 00084364); we coadded these pre-explosion images as deep templates in the UV filters. After the SN had faded significantly, we obtained Swift/UVOT Target-of-Opportunity exposures in the *U*, *B*, and *V* bands to serve as optical templates. We performed aperture photometry with `HEASoft/uvotsource` using a 5″ radius and subtracted the host-galaxy background measured with the template images. The results of photometry can be found in Table 1.

2.1.3. Forced Photometry of Transient Surveys

Via the public forced-photometry services, we retrieved the ZTF *g*- and *r*-band light curves and the ATLAS light curves in the cyan (*c*; 420–650 nm) and orange (*o*; 560–820 nm) bands. In addition, we also obtained the *L*-band light curve of SN 2024aecx from GOTO (the Gravitational-wave Optical Transient Observer), which is a wide-field survey facility designed to perform rapid optical follow-up of gravitational-wave events and other transient phenomena (D. Steeghs et al. 2022). The *L* band is a broad optical filter employed by GOTO, covering approximately 4000–7000 Å. By integrating over a wide spectral range, the *L* band maximizes sensitivity and is particularly well suited for the early detection and monitoring of optical transients.

2.2. Spectroscopy

We obtained optical spectroscopy of SN 2024aecx with a number of 2–10 m-class telescopes. These spectra are available online. At Xinglong Observatory, the 2.16 m reflector (XL-216) was equipped with the Beijing Faint Object Spectrograph and Camera (BFOSC), a Cassegrain spectrograph providing low-resolution spectra over the wavelength range from 3500 to 9000 Å (Z. Fan et al. 2016). The 2.0 m Himalayan Chandra Telescope (HCT) at Hanle, outfitted with Hanle Faint Object Spectrograph Camera (HFOSC), covered 3500–9000 Å (R. Cowsik et al. 2002; T. P. Prabhu 2014). India's 3.6 m Devasthal Optical Telescope (DOT) employed ADFOSC for low-resolution spectra from 3500 to 10000 Å (R. Sagar et al. 2020). On La Palma, the 2.56 m Nordic Optical Telescope (NOT) used ALFOSC and multiple grisms to span 3200–9600 Å (A. A. Djupvik & J. Andersen 2010). The 10.4 m Gran Telescopio Canarias (GTC) at Roque de los Muchachos, equipped with OSIRIS, provided low and medium resolution spectra over the optical range (J. Cepa et al. 2000).

The first spectrum of SN 2024aecx was obtained by XL-216 as early as $t = 0.3$ day after discovery, and we took another early spectrum with the GTC at $t = 0.7$ day. After that, our spectroscopic follow-up used a cadence of one to a few days out to $t = 54.2$ day. At the nebular phase, we took three more spectra with NOT and GTC at $t = 71.5$, 123.5 and 158.4 days. The one-dimensional spectra were extracted with the data reduction packages IRAF (D. Tody 1986) and PYPEIT (J. Prochaska et al. 2020). The raw spectral images were first bias-subtracted and flat-field corrected, followed by cosmic-ray removal and wavelength calibration using comparison arc lamps. Sky background was subtracted from regions adjacent to the target trace, and the spectra were flux-calibrated with spectrophotometric standard stars observed on the same nights.

Additionally, we also used three publicly available spectra from the TNS: two epochs obtained with Gemini North's GMOS-N on the 8.1 m telescope and one from the University of Hawaii 88 inch telescope (UH88; M. A. Tucker et al. 2022) (J. Andrews et al. 2024a, 2024b; J. Hinkle 2024). Table 2 shows a log of all spectroscopic observations used in this work.

2.3. Hubble Space Telescope/Advanced Camera for Survey and Very Large Telescope /Multi Unit Spectroscopic Explorer Archive Data

The host galaxy of SN 2024aecx, NGC 3521, has been observed by the Advanced Camera for Survey (ACS) on the Hubble Space Telescope (HST) and the Multi Unit Spectroscopic Explorer (MUSE) on the Very Large Telescope (VLT). The fields of view of the HST/ACS and VLT/MUSE observations, along with the explosion site of SN 2024aecx, are shown in Figure 1.

The HST/ACS observations (Program ID: GO-17502; PI: D. Thilker) imaged the outskirt of NGC 3521 with exposure times of 1610s in the F606W band and 2110s in the F814W band. The data can be found in MAST doi:10.17909/9dfy-qz66. In this work, we will make use of these images to determine the distance to the host galaxy using the tip of the red giant branch (TRGB) method (Section 3.1). The data were retrieved from the Mikulski Archive for Space Telescopes[24] and details of data reduction will be described in Section 3.1.

VLT/MUSE provides integral-field-unit (IFU) spectroscopy over a 1×1 arcmin^2 field, spanning 4650–9300 Å (R. Bacon et al. 2010). This wavelength range includes the principal nebular emission lines—Hα, Hβ, [O III] $\lambda\lambda$4959, 5007, and [N II] $\lambda\lambda$6548, 6583—from which gas-phase metallicity can be derived using strong-line diagnostics (B. E. J. Pagel et al. 1979;

[24] https://archive.stsci.edu/

Table 2
Spectroscopic Observation Log of SN 2024aecx

MJD	Epoch[a] (day)	Filter	Grism/VPH	Spectral Range (Å)	Resolution (R)[b]	Telescope/Instrument
60660.9	0.3	385LP	G4	3700–8800	∼1300	XL-216/BFOSC
60661.2	0.7	⋯	R2500U	3440–4610	∼2500	GTC/OSIRIS+
			R2500V	4500–6000	∼2500	
			R1000R	5100–10000	∼1000	
60661.6	1.0	⋯	B480+_G5309	3700–7500	∼1500	Gemini-N/GMOS[c]
60661.6	1.0	⋯	B+R	3200–5200, 5100–9700	∼1000, ∼1300	UH88/SNIFS[d]
60661.8	1.2	385LP	G4	3700–8800	∼1300	XL-216/BFOSC
60662.9	2.3	385LP	G4	3700–8800	∼1300	XL-216/BFOSC
60663.6	3.0	⋯	B480+_G5309	3750–7500	∼1500	Gemini-N/GMOS[e]
60666.9	6.3	385LP	G4	3700–8800	∼1300	XL-216/BFOSC
60667.9	7.3	385LP	G4	3700–8800	∼1300	XL-216/BFOSC
60670.9	10.3	385LP	G4	3700–8800	∼1300	XL-216/BFOSC
60671.9	11.3	385LP	G4	3700–8800	∼1300	XL-216/BFOSC
60672.2	11.6	⋯	Grism #4	3200–9600	∼710	NOT/ALFOSC
60672.9	12.3	385LP	G4	3700–8800	∼1300	XL-216/BFOSC
60674.0	13.4	⋯	Gr. 7, Gr. 8	3800–6840, 5800–8350	∼1300, ∼2200	HCT/HFOSC
60674.9	14.3	385LP	G4	3700–8800	∼1300	XL-216/BFOSC
60675.7	15.1	385LP	G4	3700–8800	∼1300	XL-216/BFOSC
60676.9	16.3	385LP	G4	3700–8800	∼1300	XL-216/BFOSC
60678.9	18.3	385LP	G4	3700–8800	∼1300	XL-216/BFOSC
60679.8	19.3	385LP	G4	3700–8800	∼1300	XL-216/BFOSC
60680.7	20.2	385LP	G4	3700–8800	∼1300	XL-216/BFOSC
60681.9	21.3	385LP	G4	3700–8800	∼1300	XL-216/BFOSC
60682.8	22.3	385LP	G4	3700–8800	∼1300	XL-216/BFOSC
60683.9	23.3	385LP	G4	3700–8800	∼1300	XL-216/BFOSC
60689.8	29.3	385LP	G4	3700–8800	∼1300	XL-216/BFOSC
60690.8	30.3	385LP	G4	3700–8800	∼1300	XL-216/BFOSC
60695.0	34.4	⋯	676R—420 gr/mm	3500–8950	∼1160	DOT/ADFOSC
60696.9	36.3	385LP	G4	3700–8800	∼1300	XL-216/BFOSC
60700.1	39.6	⋯	Grism #4	3200–9600	∼710	NOT/ALFOSC
60703.1	42.5	⋯	676R—420 gr/mm	3500–8950	∼1160	DOT/ADFOSC
60706.0	45.4	⋯	676R—420 gr/mm	3500–8950	∼1160	DOT/ADFOSC
60713.2	52.7	⋯	676R—420 gr/mm	3500–8950	∼1160	DOT/ADFOSC
60714.7	54.2	385LP	G4	3700–8800	∼1300	XL-216/BFOSC
60732.0	71.5	⋯	Grism #4	3200–9600	∼710	NOT/ALFOSC
60784.0	123.5	⋯	R1000R	5100–10000	∼1000	GTC/OSIRIS+
60818.9	158.4	⋯	R1000R	5100–10000	∼1000	GTC/OSIRIS+

Notes.
[a] Epoch in days relative to discovery.
[b] Resolving power $R \equiv \lambda/\Delta\lambda$, listed as typical values.
[c] J. Andrews et al. (2024b).
[d] J. Hinkle (2024).
[e] J. Andrews et al. (2024a).

M. G. Edmunds & B. E. J. Pagel 1984). Such capabilities make VLT/MUSE exceptionally suited to probing the chemical properties of SN host regions. For NGC 3521, VLT/MUSE obtained a deep 4500s exposure (Program ID: 099.B-0242, 098.B-0551; PI: C.M. Carollo) centered on the nucleus, and the field of view encompasses the SN explosion site. The VLT/MUSE data were retrieved from the ESO Science Archive.[25] Details of data reduction will be described in Section 3.2.

3. Host Galaxy

SN 2024aecx is located in the central region of the nearby galaxy NGC 3521, a late-type spiral galaxy that is closely analogous to the Milky Way (Figure 1). In this section, we try to constrain the distance, metallicity, and extinction of the host galaxy, which are important for the analysis of SN 2024aecx.

3.1. Distance

There are 26 redshift-independent distance measurements for NGC 3521, all based on the Tully–Fisher method, according to the NASA/IPAC Extragalactic Database.[26] The reported distances, however, span a very large range from 4.0 to 16.4 Mpc. In this work, we use the HST/ACS imaging observations of NGC 3521 (Figure 1; Section 2.3) and apply the TRGB method (W. Baade 1944; A. Sandage 1971; G. S. Da Costa &

[25] https://archive.eso.org/scienceportal/home

[26] https://ned.ipac.caltech.edu/

T. E. Armandroff 1990; M. G. Lee et al. 1993) to secure a more accurate measurement. This method is based on the fact that low-mass stars climbing the RGB reach a nearly fixed luminosity just before core helium ignition. Therefore, one can derive a precise distance by identifying the sharp cutoff in the observed luminosity function of RGB stars (i.e., the tip) and comparing its apparent magnitude with the well-calibrated TRGB absolute magnitude. This technique is relatively insensitive to metallicity and crowding effects, allowing for robust distance measurements for nearby galaxies.

We followed the same approach as described by G. Anand et al. (2020) to implement the TRGB distance measurement. We first performed PSF photometry on the HST/ACS images with the DOLPHOT (A. Dolphin 2016) package, and then applied several quality cuts to construct a clean sample of stellar sources:

$$\mathtt{snr}_{\mathrm{F606W}} > 5, \tag{1}$$

$$\mathtt{snr}_{\mathrm{F814W}} > 5, \tag{2}$$

$$\mathtt{crowd}_{\mathrm{F606W}} + \mathtt{crowd}_{\mathrm{F814W}} < 0.8, \tag{3}$$

$$(\mathtt{sharp}_{\mathrm{F606W}} + \mathtt{sharp}_{\mathrm{F814W}})^2 < 0.075, \tag{4}$$

where snr, crowd, and sharp are DOLPHOT-reported quality parameters on the signal-to-noise ratio, crowding, and sharpness of the detected sources. The color–magnitude diagram of the stellar sample is shown in Figure 2 (top), where the RGB stars from NGC 3521 are clearly visible.

We carried out artificial-star tests in both the F606W and F814W bands to assess the photometry accuracy and detection limit. Different input magnitudes were considered, ranging from 25.0 to 28.7 mag (25.0 to 28.0 mag) for the F606W (F814W) band. For each magnitude, 6000 artificial stars were randomly injected across the field and we tried to recover the artificial stars with DOLPHOT. The probability of recovering sources above the 5σ threshold varies with the input magnitude, which can be fitted with a Gaussian error function. We defined the detection limit as the magnitude where the probability declines to 50%. The recovered magnitudes exhibit no systematic bias from the input magnitudes, but the scatters are systematically (but only slightly) larger than the nominal photometric errors reported by DOLPHOT. We applied a scaling factor to correct the photometric errors in our stellar sample.

We binned the F814W magnitudes in intervals of 0.05 mag to construct the luminosity function, which was then smoothed using a Savitzky–Golay filter (window length of seven bins and a quadratic polynomial fit) (A. Savitzky & M. J. E. Golay 1964) to suppress shot noise while preserving the intrinsic discontinuity at the tip (Figure 2, bottom). A Sobel edge-detection filter ([–2, 0, +2]) was applied to the smoothed luminosity function (M. G. Lee et al. 1993). We regard the peak of the Sobel response as the TRGB magnitude and the half width at half-maximum as the uncertainty, which is 26.28 ± 0.21 mag. With this value, we derived a distance of 11.3 ± 1.1 Mpc for NGC 3521, adopting the TRGB zero-point (i.e., color calibration) of L. Rizzi et al. (2007) and incorporating systematic uncertainties associated with the zero-point as described in G. Anand et al. (2020). We have considered the Galactic extinction (D. J. Schlegel et al. 1998); internal extinction within the host galaxy is negligible for the analyzed HST/ACS field, which lies in the far galaxy outskirt. This distance is consistent, within the uncertainties, with the value of 11.40 ± 0.56 Mpc adopted by X. Zou et al. (2026).

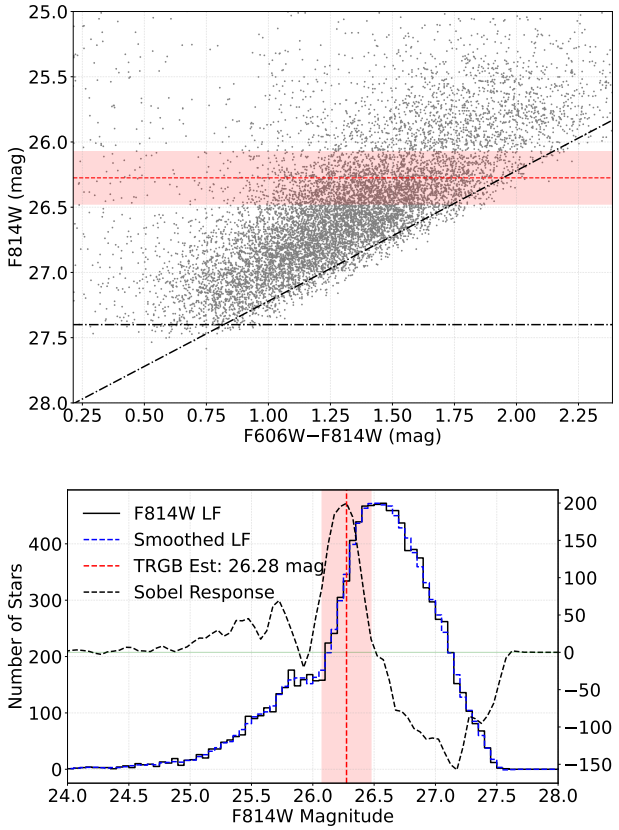

Figure 2. Top: Color–magnitude diagram of resolved stars in the outer regions of NGC 3521 from HST/ACS imaging. Each gray point represents an individual star, plotted in F814W versus F606W–F814W. The red dashed line marks the measured TRGB at $\mathrm{F814W}_0 = 26.28$ mag, and the shaded band denotes its $\pm 1\sigma$ uncertainty. The black dashed–dotted line indicates the approximate 50% completeness limit. Bottom: F814W luminosity function of the observed stars (solid black histogram) together with its smoothed version (blue dashed line). The red vertical dashed line and shaded region again show the TRGB and its uncertainty. Overlaid in black (right-hand axis) is the Sobel edge-detection response, whose peak identifies the TRGB.

3.2. Metallicity

In this section we try to derive the metallicity of SN 2024aecx based on VLT/MUSE IFU spectroscopy. We processed the VLT/MUSE datacube with the IFUANAL package (J. D. Lyman et al. 2018), following the same methodology of N.-C. Sun et al. (2022, 2023b) and Q. Xi et al. (2025). First, the datacube was deredshifted and corrected for Galactic extinction. The spaxels were then adaptively binned using a Voronoi tessellation scheme until achieving a continuum signal-to-noise ratio of at least 120 over the 5590–5680 Å interval. In each Voronoi bin, the combined spectrum was fitted for its stellar continuum with the STARLIGHT package (R. Cid Fernandes et al. 2005), employing G. Bruzual & S. Charlot's (2003) simple stellar population models. Our library comprised 60 base models spanning 15 ages (3 Myr–13 Gyr) and four metallicities ($Z = 0.004$, 0.008, 0.02, 0.05). The best-fit stellar continuum in each bin was then scaled appropriately and subtracted from the observed spectra at the individual spaxel level.

Figure 3 (top) shows a map of Hα integrated flux, which is calculated with the 0th momentum. The observed field is full

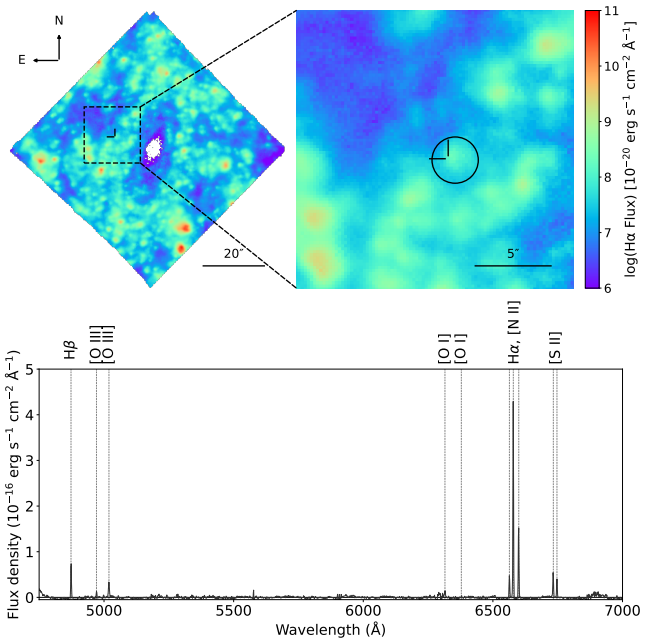

Figure 3. Top: VLT/MUSE Hα flux map of the environment of SN 2024aecx in NGC 3521, calculated from the 0th moment of the datacube and shown on a logarithmic scale. The black cross marks the SN position and the circle outlines the local H II region, within which we extracted a spectrum for analysis (see text). North is up and east is left. Bottom: Continuum-subtracted spectrum extracted from the aperture.

of ionized gas, suggesting very active star formation. The position of SN 2024aecx coincides with a circular H II region with a radius of $R = 80$ pc. We coadded spectra from all spaxels within this region and the stacked spectrum is displayed in the bottom panel of Figure 3. The spectrum exhibits the strong Balmer lines of Hα (λ6563) and Hβ (λ4861) as well as prominent forbidden transitions of [O III] $\lambda\lambda$4959, 5007, [N II] $\lambda\lambda$6548, 6583, and [S II] $\lambda\lambda$6716, 6731. In contrast, the lines of [O I] $\lambda\lambda$6300 6363 are very faint. We fitted each line with a Gaussian function to measure its integrated flux.

We estimated the gas-phase metallicity with the strong-line method based on the O3N2 calibration of R. A. Marino et al. (2013)

$$12 + \log(\mathrm{O/H}) = 8.533 - 0.214 \times \mathrm{O3N2},$$

where

$$\mathrm{O3N2} = \log\left(\frac{[\mathrm{O\ III}]\,\lambda5007}{\mathrm{H}\beta}\right) - \log\left(\frac{[\mathrm{N\ II}]\,\lambda6584}{\mathrm{H}\alpha}\right).$$

Applying this calibration to our measured line ratios, we derived an oxygen abundance of $12 + \log(\mathrm{O/H}) = 8.49 \pm 0.18$ dex, which is very close to the solar value (8.69 dex, M. Asplund et al. 2009).

3.3. Extinction

The Galactic extinction toward NGC 3521 is $A_V^{\mathrm{MW}} = 0.144$ mag according to the D. J. Schlegel et al. (1998) all-sky dust map. We employed three different methodologies to derive the internal extinction of SN 2024aecx due to interstellar dust within the host galaxy. For simplicity, we assume a J. A. Cardelli et al. (1989) standard extinction law with $R_V = 3.1$.

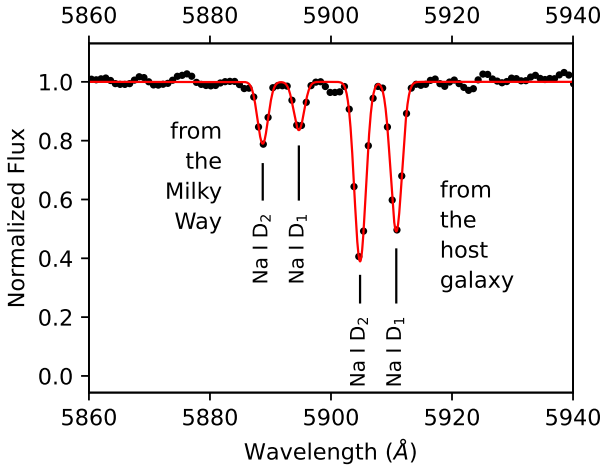

Figure 4. Normalized GTC spectrum of SN 2024aecx obtained at $t = 0.7$ day, showing prominent Na I D absorption features. Black circles are the observed data, and the red curves are Gaussian fits to each line. The left component arises from the Milky Way, while the right component is from the host galaxy.

3.3.1. Balmer Decrement

As described in Section 3.2, SN 2024aecx is spatially coincident with an HII region. Its VLT/MUSE spectrum (Figure 3) allows us to estimate an extinction with the Balmer-decrement method. The observed flux ratio of Hα/Hβ is 5.33 while the intrinsic flux ratio should be close to 2.87 (D. E. Osterbrock & G. J. Ferland 2006). From this, we derived an extinction of $A_V^{\mathrm{Host}} = 1.95$ mag. It should be noted, however, that the Balmer-decrement extinction corresponds to that for the ionized gas and could be different from that for the SN if there is dust between them along the line of sight (e.g., N.-C. Sun et al. 2021).

3.3.2. Na I D Absorption

At $t = 0.7$ day, we obtained a deep spectrum with the GTC telescope (see Sections 2 and 5), where the Na I D absorption features are clearly resolved. As shown in Figure 4, there are two components of Na I D absorption, one close to the doublet's rest wavelengths and one at a higher redshift of $z = 0.0025$ that is consistent with NGC 3521. We attribute the former to interstellar absorption within the Milky Way and the later to that in the host galaxy. We modeled the continuum as a constant and fitted each line with a Gaussian profile. The total equivalent width (EW) of the host-galaxy Na I D doublet is $\mathrm{EW}^{\mathrm{Host}} = (1.21 \pm 0.03)$ Å $+(1.45 \pm 0.03)$ Å $= 2.65 \pm 0.04$ Å, consistent with the measurement of X. Zou et al. (2026).

A number of works reported empirical relations between the Na I D absorption and interstellar extinction/reddening (e.g., M. Turatto et al. 2003; D. Poznanski et al. 2012; M. D. Stritzinger et al. 2018). The host-galaxy Na I D EW is outside the dynamical range of the relation of D. Poznanski et al. (2012) (which has a maximum value of EW = 2.4 Å) and applying their relation will lead to an unphysically large value of extinction. We can derive an extinction of $A_V^{\mathrm{Host}} = 2.1$ mag based on M. D. Stritzinger et al. (2018); however, there is significant scatter in their relation and the derived value could have a large uncertainty. M. Turatto et al. (2003) found two branches in the relation between reddening and Na I D EW (their Figure 3). Adopting the lower branch, we infer a host extinction of $A_V^{\mathrm{Host}} = 1.3$ mag for SN 2024aecx.

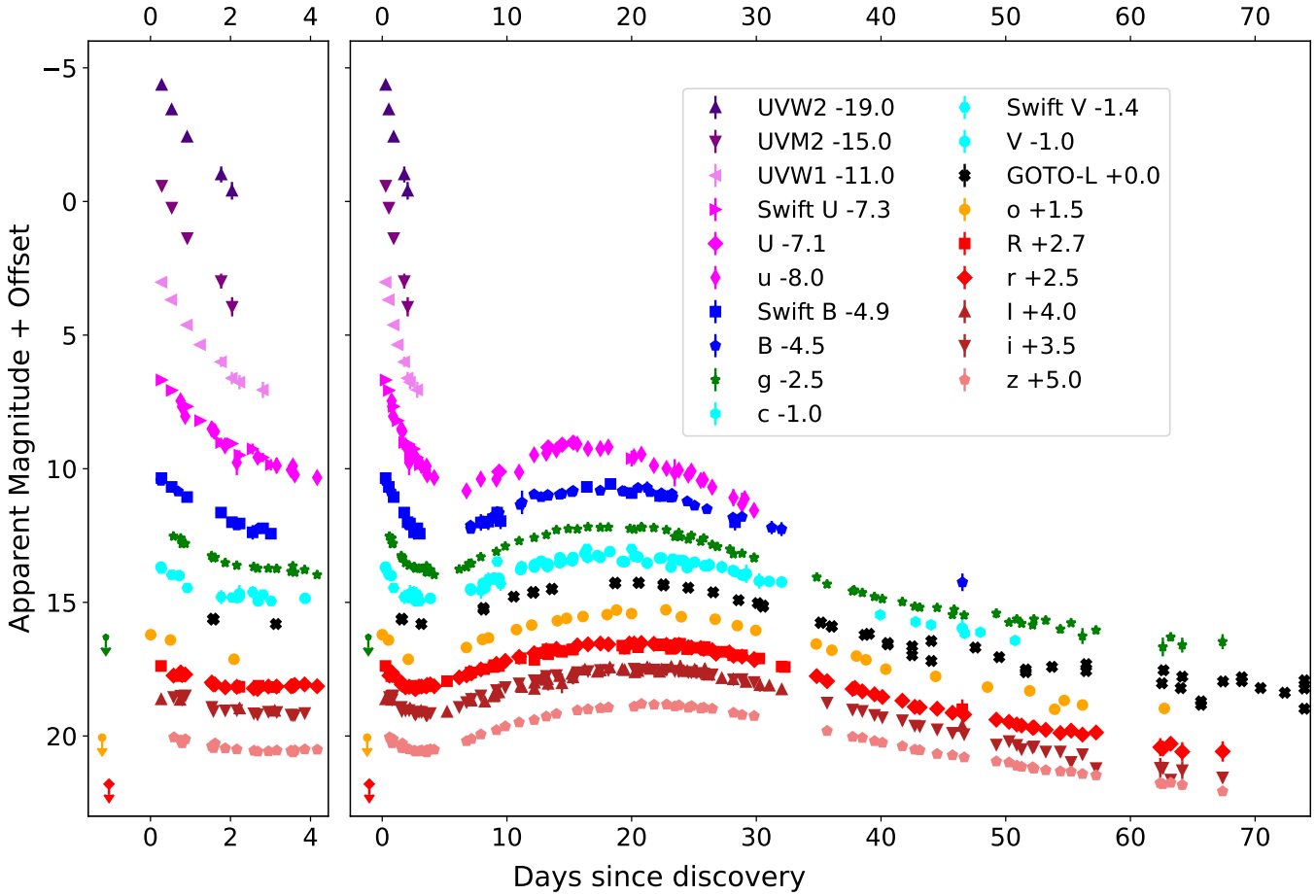

Figure 5. Multiband light curves of SN 2024aecx. Each filter is shifted vertically for clarity. Error bars denote 1σ photometric uncertainties.

Ó. Rodríguez et al. (2023) presented an empirical relation between the host-galaxy extinction of SESNe and the equivalent width of the Na I D absorption feature, $E(B-V) = (0.007 \pm 0.024) + (0.246 \pm 0.054)\,\mathrm{EW}_{\mathrm{Na\,I\,D}}$ [Å], with an intrinsic scatter $\hat{\sigma} = 0.094$ mag. Substituting $\mathrm{EW}_{\mathrm{Na\,I\,D}} = 2.7$ Å gives $E(B-V) = 0.007 + 0.246 \times 2.7 = 0.67$ mag. Propagating the coefficient uncertainties together with the intrinsic scatter yields $\sigma_{E(B-V)} \approx 0.18$ mag, i.e., $E(B-V) = 0.67 \pm 0.18$ mag. However, the fit exhibits substantial intrinsic dispersion, and the calibration sample in Ó. Rodríguez et al. (2023) covered only $\mathrm{EW}_{\mathrm{Na\,I\,D}} \approx 0$–1 Å, well below our measurement; consequently, this extrapolated estimate may not be reliable.

3.3.3. Comparison with Template Color

One can also derive extinction by comparing the observed SN color curves with well-established templates (M. D. Stritzinger et al. 2018). With this method, we obtained $A_V^{\mathrm{Host}} = 1.2$ mag, the details for which will be described later in Section 4.1. This value is very close to the result based on Na I D absorption and is adopted for subsequent analysis. The value is much smaller than that based on Balmer decrement, suggesting that there is a non-negligible amount of dust along the line of sight between SN 2024aecx in the foreground and the ionized gas in the background.

4. Light Curve

Figure 5 presents the UV–optical multiband light curves of SN 2024aecx. The last nondetection by ATLAS is at $t = -1.2$ days with a detection limit of $o > 18.56$ mag while the last nondetections by ZTF are at $t = -1.1$ days with $g > 18.8$ mag and $t = -1.0$ day with $r > 19.3$ mag. This suggests that SN 2024aecx was discovered shortly after its explosion, likely within 1 day. At $t \sim 0$ day, SN 2024aecx appears to be very bright and blue, with strong emission in the UV filters. During the next few days, the flux decreases swiftly across all bands, with steeper declines in the bluer filters and more gradual fading at redder wavelengths. Such behavior is characteristic of the shock-cooling emission observed in Type IIb SNe, as exemplified by SN 1993J, SN 2011dh, and SN 2016gkg (B. P. Schmidt et al. 1993; M. Ergon et al. 2014; L. Tartaglia et al. 2017).

Following the shock-cooling phase, SN 2024aecx falls below the detection limit in the UV filters (Swift/UVOT W2, M2, and W1) while in the optical bands it rises again to a broad second maximum. The u band peaks at $t \simeq 15$ days, while the r, i, and z bands reach their maxima later at $t \simeq 20$ days. The systematically longer rise times at redder wavelengths reflect the increased photon diffusion time through the cooler, more opaque ejecta (F. Taddia et al. 2018). After the main peak, the light curves gradually decline out to 70 days post discovery.

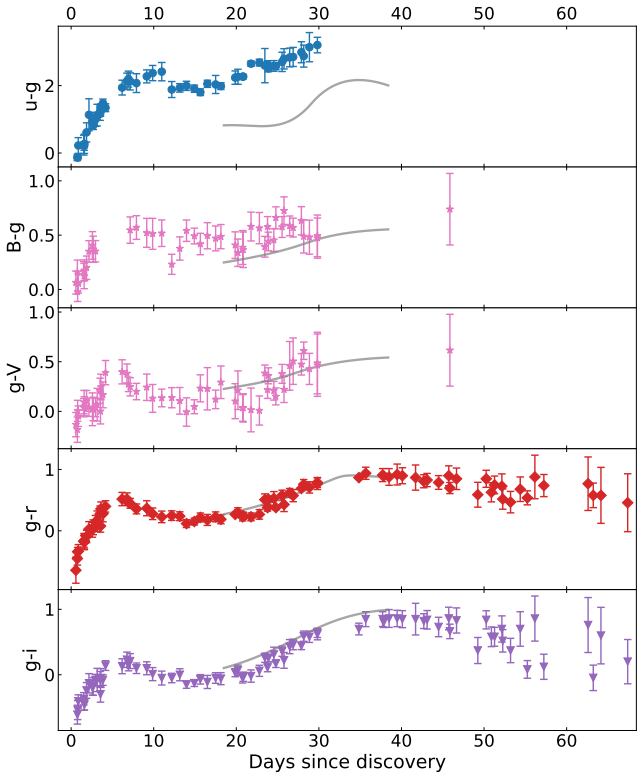

Figure 6. Color evolution of SN 2024aecx after correcting for the Galactic and host extinctions ($A_V^{\rm tot} = 1.34$). The orange lines are template color curves for Type IIb SNe (M. D. Stritzinger et al. 2018).

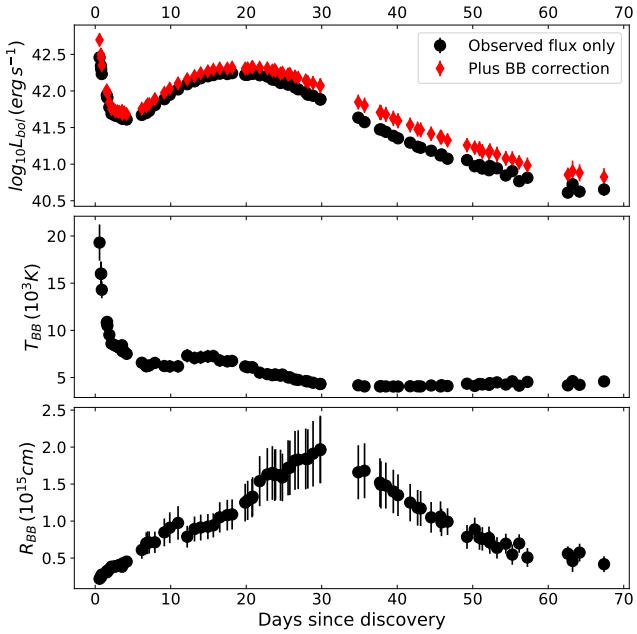

Figure 7. Bolometric evolution of SN 2024aecx derived with the SUPERBOL code. Top: Logarithmic bolometric luminosity $L_{\rm bol}$ from the observed flux only (black circles) and after applying the blackbody correction (red diamonds). Middle: Blackbody temperature $T_{\rm BB}$ in units of 10^3 K. Bottom: Blackbody radius $R_{\rm BB}$ in units of 10^{15} cm. All quantities are plotted as a function of days since discovery.

(The data used to create this figure are available in the online article.)

4.1. Color Evolution

Figure 6 shows the $X - g$ or $g - X$ ($X = u, B, V, r, i$) color curves of SN 2024aecx in comparison to the M. D. Stritzinger et al. (2018) template of Type IIb SNe, which covers 20 days from the V-band maximum. In constructing the color curves, we have interpolated the epochs of photometry in each band with respect to those in the g band.

The observed colors are much redder than the template even after correcting for a Galactic extinction of $A_V = 0.144$ mag (D. J. Schlegel et al. 1998; Section 3.3). This suggests that SN 2024aecx suffers from significant interstellar dust reddening within the host galaxy. We fitted the color curves with the least-square method by varying the host extinction; under the assumption of a standard J. A. Cardelli et al. (1989) extinction law with $R_V = 3.1$, the observed colors match the template best with a host extinction of $A_V^{\rm Host} = 1.2$ mag. This value is very consistent with that derived with Na I D absorption (1.3 mag; see Section 3.3).

Note that, however, the $u - g$ color still appear much redder than the template after correcting for the Galactic and host extinction. We tested by changing R_V in the extinction law and refitting the color curves; in all cases, no better match can be found. We speculate that this is due to some strong absorption (e.g., from the iron-group elements), which makes SN 2024aecx very faint in the u band.

During the shock-cooling phase, SN 2024aecx shows a very blue color ($g - r = -0.6$ mag) at $t \sim 0$ day, followed by a rapid blue-to-red evolution to $g - r = 0.5$ mag at $t = 4$ days. After that, it again turns bluer until $g - r = 0.1$ mag near maximum at $t = 15$ days, and then evolves redward after maximum. From $t = 35 \sim 40$ days, SN 2024aecx starts to slowly evolve blueward. This color evolution is similar to those observed for other Type IIb SNe (B. P. Schmidt et al. 1993; B. Kumar et al. 2013; M. Ergon et al. 2014; A. Morales-Garoffolo et al. 2014, 2015; L. Tartaglia et al. 2017; M. D. Stritzinger et al. 2018; B. M. Subrayan et al. 2025).

4.2. Bolometric Light Curve

We employed the SUPERBOL package (M. Nicholl 2018) to reconstruct the UV–optical (pseudo)bolometric light curve. In doing this, we have adopted a distance of $D = 11.3$ Mpc, a Galactic extinction of $A_V^{\rm MW} = 0.144$ mag, a host extinction of $A_V^{\rm Host} = 1.2$ mag, and a standard extinction law of J. A. Cardelli et al. (1989) with $R_V = 3.1$ (see Section 3). The results are shown in Figure 7.

At $t = 0$ d, SN 2024aecx has a very high bolometric luminosity of $\log(L_{\rm bol}/{\rm erg\ s^{-1}}) \gtrsim 42.5$ and blackbody temperature of $T_{\rm BB} \sim 20,000$ K. At $t = 4$ d, the bolometric luminosity declines to a local minimum of $\log(L_{\rm bol}/{\rm erg\ s^{-1}}) \sim 41.7$ while the blackbody temperature cools down to $T_{\rm BB} = 7510$ K. After the shock-cooling phase, the bolometric luminosity climbs up to the main peak with $\log(L_{\rm bol}/{\rm erg\ s^{-1}}) \sim 42.2$ at $t = 20$ days and then gradually decreases; the blackbody temperature reaches the second local maximum with $T_{\rm BB} = 7300$ K at $t = 15$ days, after which it cools down continuously. The blackbody radius follows an almost linear evolution with time before and after a peak of $R_{\rm BB} = 2 \times 10^{15}$ cm at $t = 30$ days. It should be noted that, after the main peak, a significant portion of the SN radiation may lie at infrared wavelengths outside our observed UV and optical filters. In constructing the bolometric light curve, the code fits a blackbody spectral energy distribution (SED) to the multiband UV–optical fluxes at each epoch, and the near-infrared (NIR) contribution is obtained by interpolating this best-fitting blackbody SED. In our case, the inferred NIR

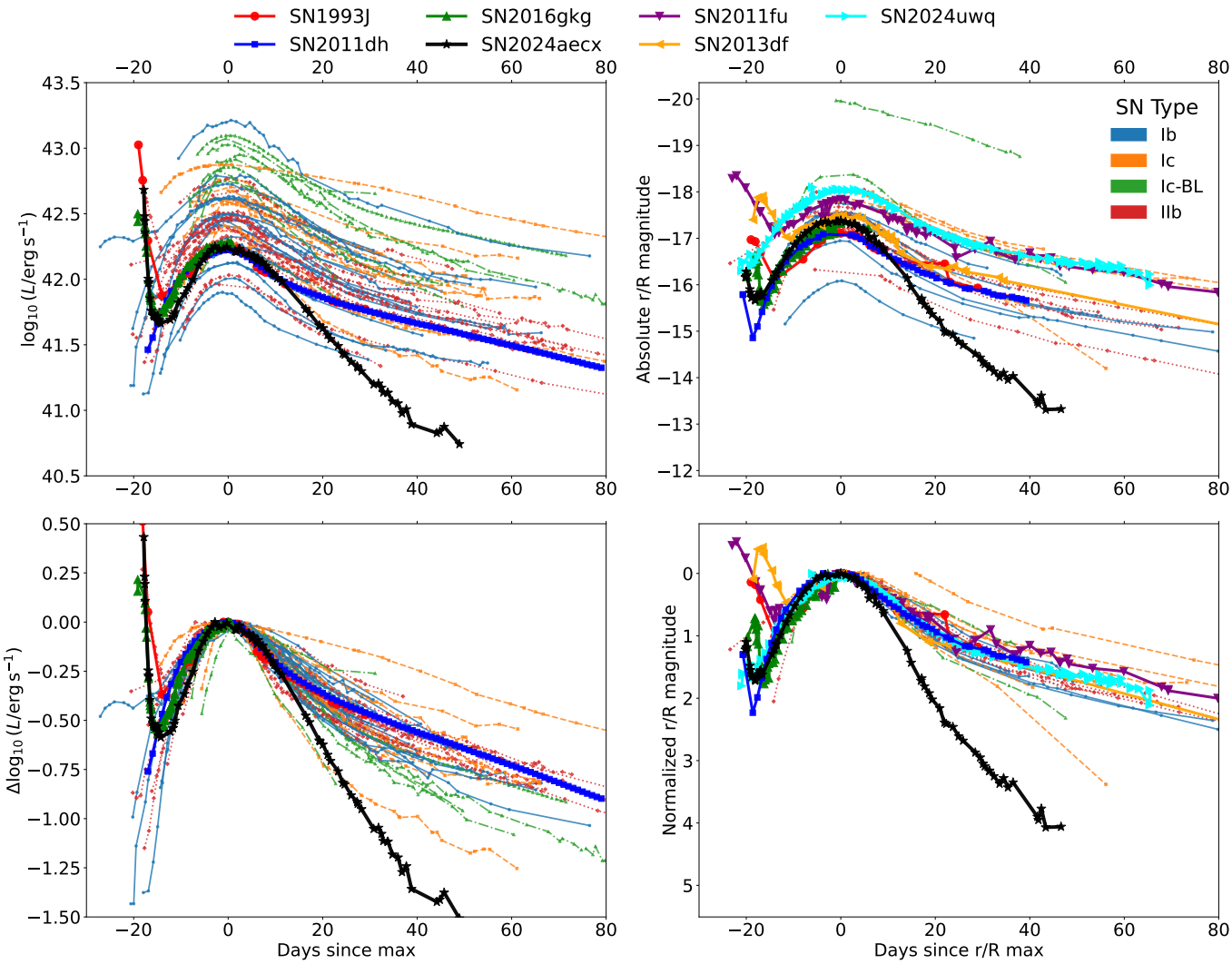

Figure 8. Left: Bolometric light curves for SN 2024aecx (black stars) and a sample of SESNe, with the top panel showing absolute luminosities and the bottom panel showing the same curves normalized to their peaks. Right: r/R-band light curves for SN 2024aecx (black stars) and the same SESNe sample, with the top panel showing absolute magnitudes and the bottom panel showing the normalized curves. All epochs are relative to days since maximum. The bolometric light curves are drawn from J. D. Lyman et al. (2016) and F. Taddia et al. (2018) while the r-band light curves are taken from F. Taddia et al. (2018).

flux contributes about 30% of the total flux in the late time, so its omission has only a minor effect on the derived explosion parameters.

4.3. Comparison with Other SNe

Figures 8 compare the (pseudo)bolometric light curve and the r/R-band light curve of SN 2024aecx with those of other SESNe. In particular, we show three well-studied Type IIb events SN 1993J, SN 2011dh, and SN 2016gkg (B. P. Schmidt et al. 1993; I. Arcavi et al. 2011; L. Tartaglia et al. 2017), which are highlighted in the figures. For the other SESNe, the bolometric light curves are drawn from J. D. Lyman et al. (2016) and F. Taddia et al. (2018) while the r-band light curves are taken from F. Taddia et al. (2018). To facilitate a direct comparison of their temporal behavior, we also present normalized light curves whose peak logarithmic luminosities (or peak magnitudes) are set to zero.

Before SN 2024aecx, some Type IIb SNe are also found to have early peaks (e.g., SN 1993J, SN 2011dh, SN 2011fu, SN 2013df, SN 2016gkg and SN 2024uwq; B. P. Schmidt et al. 1993; B. Kumar et al. 2013; M. Ergon et al. 2014; A. Morales-Garoffolo et al. 2014, 2015; L. Tartaglia et al. 2017; B. M. Subrayan et al. 2025), while other SNe of this class do not show obvious signs of early shock-cooling emission. Compared with them, SN 2024aecx has one of the most prominent early shock-cooling peaks. The luminosity of the first peak [$\log(L_{\rm bol}/{\rm erg\ s^{-1}}) \gtrsim 42.5$] and the change of luminosity until the dip ($\Delta \log(L_{\rm bol}/{\rm erg\ s^{-1}}) \sim 1.0$ dex) both have the largest values for Type IIb SNe. The duration of the first peak is also very short ($\sim$4 days) compared with other Type IIb SNe.

The bolometric luminosity and r-band absolute magnitude of the main peak of SN 2024aecx are relatively low but still within the observed ranges of Type IIb SNe. However, the rise to the main peak and the postpeak decline are markedly fast compared with other SESNe. This is most obvious in the normalized r-band light curve (Figure 8, right), which shows that the r-band magnitude fades by approximately $\sim$4 mag over just 40 days. The reason for this rapid evolution will be discussed further in Section 6.

5. Spectroscopy

5.1. Photosphere Phase Spectrum

Figures 9 and 10 shows the complete spectral sequence of SN 2024aecx (uncorrected for redshift or extinction), spanning from the earliest postexplosion epoch to the nebular phase. At the earliest epochs of $t = 0.3$–1.2 days, SN 2024aecx displays a hot, blue, and nearly featureless continuum with only Na I D absorptions. Its early-time appearance closely resembles other young SNe (e.g., SN 2011dh and SN 2016gkg; I. Arcavi et al. 2011; L. Tartaglia et al. 2017). Using the Na I D absorption in SN 2024aecx, we infer the host-galaxy extinction as detailed in Section 3.3.

From $t = 2.3$ days, the SN spectra develop pronounced P-Cygni profiles in Ca II H&K: $\lambda\lambda$ 3933.66, 3968.47 Å, Ca II IR triplet: $\lambda\lambda$8498.02, 8542.09, 8662.14 Å, the Mg II λ4481, and the Fe II $\lambda\lambda$4924, 5018, 5169 triplet. There is also a P-Cygni feature associated with He I λ5876, which is possibly blended with the Na I D lines. There are some weak features at the wavelength of Hα, which is, however, very easily confused with Si II λ6355. X. Zou et al. (2026) used SYNAPPS synthesis and suggested that this feature arises primarily from both Hα and Si II. This confirms SN 2024aecx to be a Type IIb event.

We modeled the absorption minima of the P-Cygni profiles using Gaussian functions to derive the velocity evolution of the spectral lines (shown in Figure 11). Initially, the velocities of all spectral lines decrease with time. The Ca II infrared triplet and Hα exhibits the highest velocity, reaching $\sim$12,000 km s^{-1}. This is followed by He I λ5876 and the Fe II triplet, both peaking at nearly 10,000 km s^{-1}. The Mg II λ4481 line shows the lowest velocity, starting at approximately 7000 km s^{-1} and declining thereafter. The different velocities measured at the same epoch reflect the stratification of the ejecta: strong lines such as Hα and Ca II IR triplet form in the fast outer layers, whereas weaker lines like Fe II and Mg II arise deeper in the ejecta where the velocity is lower (L. Dessart et al. 2015). After approximately 20 days, the He I λ5876 velocity exhibits a gradual increase, which may be attributed to blending with Na I D or the presence of a complex, multicomponent velocity structure rather than a single kinematic component. Since we modeled each absorption trough with a single Gaussian component, the inferred velocities may be biased in cases of line blending, particularly for Hα and He I. Typical uncertainties on the velocity measurements are $\sim$1000 km s^{-1}. For lines that may suffer from blending, we did not attempt deblending and instead fit a single Gaussian profile (e.g., Hα potentially blended with Si lines, and He I λ5876 with Na I D).

5.2. Nebula Phase Spectrum

After approximately 70 days, the SN becomes optically thin and enters the nebular phase, exhibiting prominent [O I] $\lambda\lambda$6300, 6363, [Ca II] $\lambda\lambda$7291, 7324, and the Ca II infrared triplet $\lambda\lambda$8498, 8542, 8662 emission lines. Figure 10 highlights the profile evolution of these lines. All three lines display a pronounced asymmetric profile with double peaks. Such structures are commonly interpreted as signatures of large-scale ejecta asphericity and/or differential internal extinction by newly formed dust within the ejecta (K. Maeda et al. 2008; S. Taubenberger et al. 2009; A. Bevan & M. J. Barlow 2016; S. B. Pandey et al. 2021; Q. Fang et al. 2022, 2024; A. Kumar et al. 2025). These diagnostics provide leverage on the explosion geometry and the onset of dust formation. We further note that the emission of the Ca II NIR triplet is strongly concentrated in the λ8662 component. This behavior is naturally understood if the triplet remains optically thick at these epochs: resonance scattering and line interlocking among the three fine-structure components redistribute photons absorbed in the λ8498 and λ8542 lines into the λ8662 transition, as shown by detailed radiative-transfer calculations for SN ejecta (e.g., A. Jerkstrand 2017).

To probe the geometry and structure of the ejecta of SN 2024aecx, we performed a multicomponent fit to the [O I] $\lambda\lambda$6300, 6363 and [Ca II] $\lambda\lambda$7291, 7324 doublets in the nebular-phase spectrum obtained with the GTC at $t = +123.5$ days. The results of this fit are presented in Figure 12 and Table 3.

Prior to fitting, the spectrum was corrected for the host galaxy's redshift ($z = 0.002665$) and dereddened using a foreground extinction of $A_V = 1.34$ mag with $R_V = 3.1$, following the extinction law of J. A. Cardelli et al. (1989). For the [O I] doublet, a local linear continuum, established by connecting the endpoints of the fitting region, was first subtracted. The resulting emission profile was subsequently modeled with a two-component Gaussian function. For each component, the profiles of the λ6300 and λ6363 lines were kinematically tied, sharing the same velocity shift and full width at half-maximum (FWHM), while their wavelength separation was fixed at the laboratory value. Allowing for the possibility that the doublet is not entirely optically thin, the flux ratio $I(\lambda6300)/I(\lambda6363)$ for each component was treated as a free parameter. The best fit reveals a narrow, blueshifted component (comp. 1 in Figure 3; velocity $v = -1945.23 \pm 24.85$ km s^{-1}, FWHM $= 2354.82 \pm 55.77$ km s^{-1}) and a broader, slightly redshifted component (comp. 2 in Figure 3; $v = 475.84 \pm 234.36$ km s^{-1}, FWHM $= 9770.33 \pm 268.43$ km s^{-1}). A single Gaussian was also included in the model to account for faint, underlying H α and neighboring [N II] emissions.

A similar procedure was applied to the [Ca II] doublet. After subtracting a local linear background, we found that the two lines of the doublet were significantly broadened and blended. Consequently, they were modeled with a single Gaussian profile. An additional Gaussian was incorporated to fit the adjacent [Ni II] λ7378 emission line. The best-fit model for the [Ca II] feature yields a velocity of $v = 829.99 \pm 31.20$ km s^{-1} and an FWHM of 5845.00 ± 106.17 km s^{-1}.

Therefore, our analysis reveals a complex kinematic structure in the nebular spectra of SN 2024aecx. The [O I] $\lambda\lambda$6300, 6364 doublet is best described by a two-component model, whereas the [Ca II] $\lambda\lambda$7291, 7324 doublet is well represented by a single component. We associate the single [Ca II] profile with the dominant, low-velocity, broad, and redshifted component of the [O I] profile (hereafter Component 2). Together, these features trace the bulk of the SN ejecta, suggesting a systematic redshift of the inner explosion region. Crucially, the FWHM of the [O I] Component 2 is substantially broader than that of the [Ca II] profile. Assuming homologous expansion ($v \propto r$), this velocity difference implies a chemically stratified ejecta, where the region of calcium synthesis is confined to the lower-velocity inner core, while the oxygen-rich material extends to higher velocities in the outer layers. This inferred "inside-out" nucleosynthetic structure is fully consistent with the canonical predictions of CCSN explosion models (S. E. Woosley & A. Heger 2007).

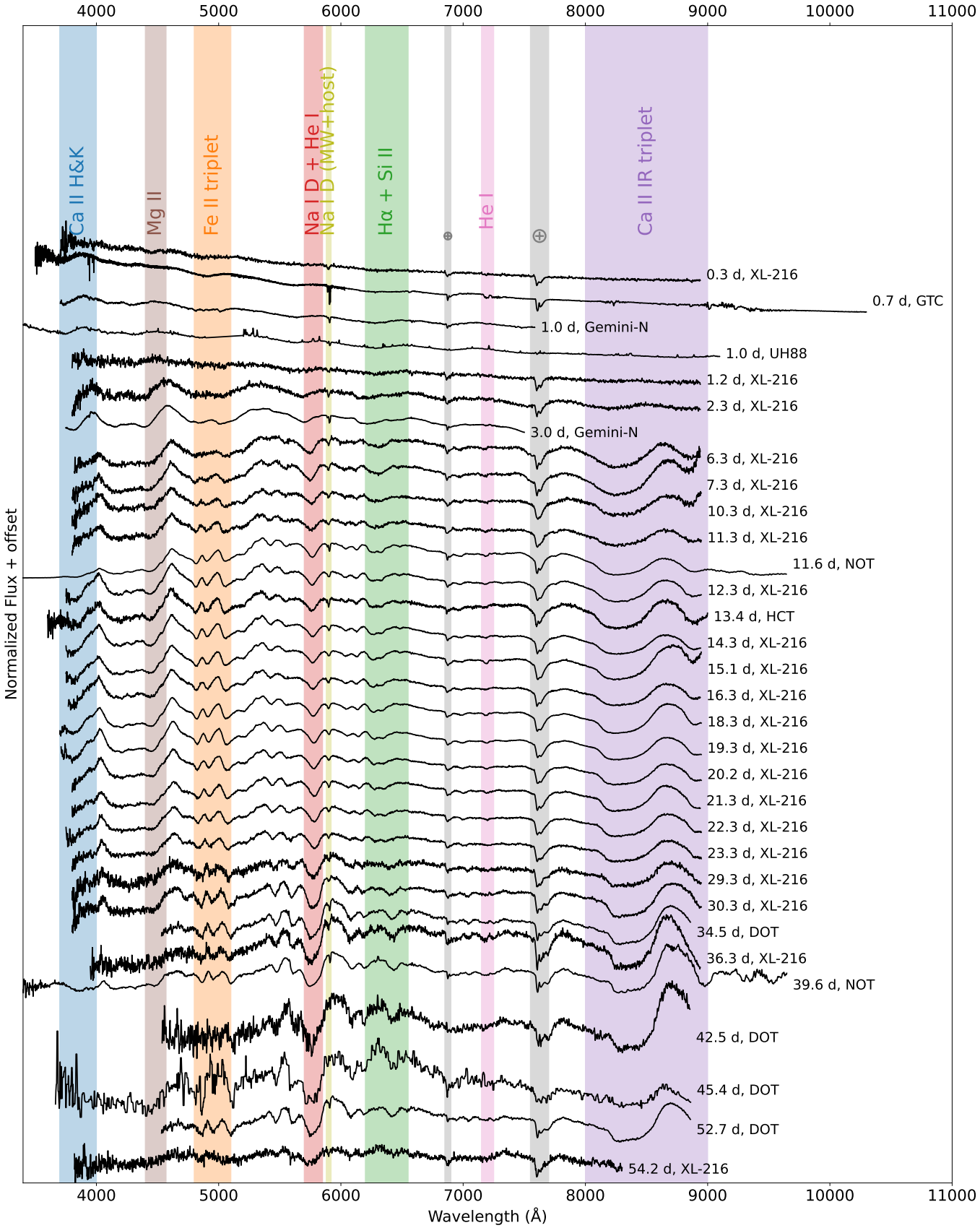

Figure 9. Flux-normalized spectra of SN 2024aecx from $t = 0.3$ day to $t = 54.2$ days (uncorrected for redshift or extinction). Major telluric bands are shaded in gray and key SN features are indicated by colored bands.

(The data used to create this figure are available in the online article.)

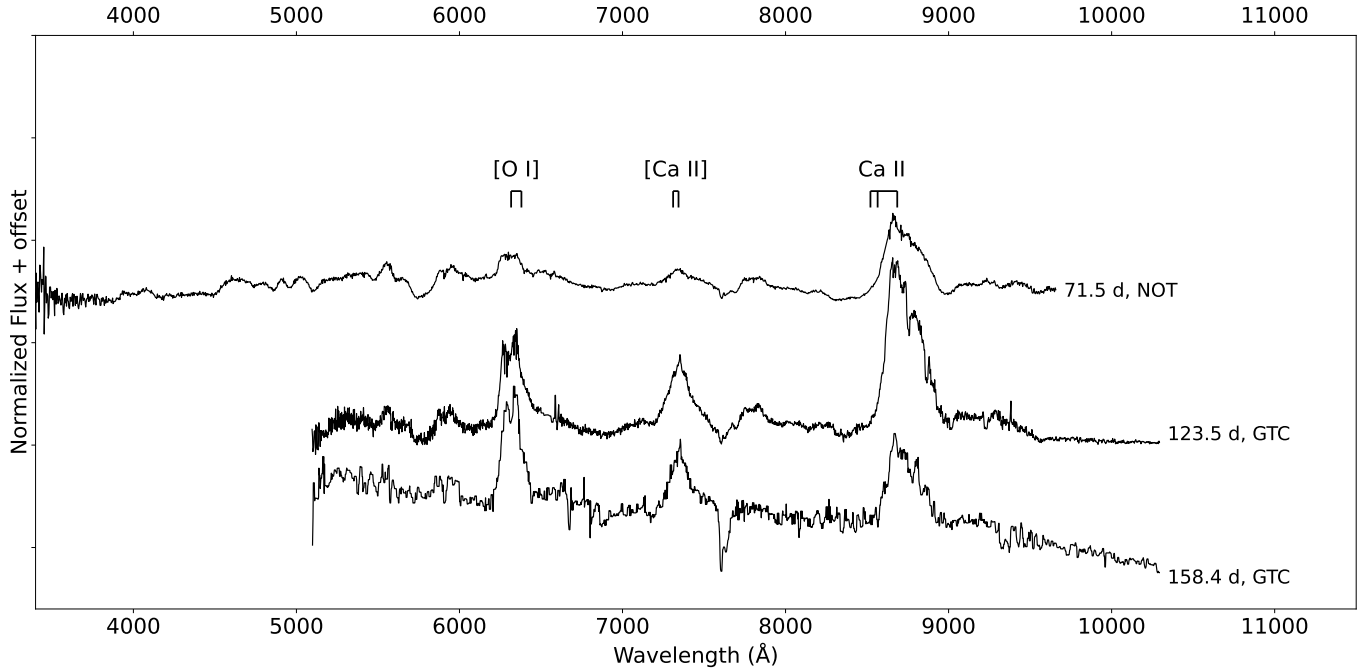

Figure 10. Nebular-phase spectra of SN 2024aecx at 71.5, 123.5, and 158.4 days (uncorrected for redshift or extinction), with the main emission lines marked.

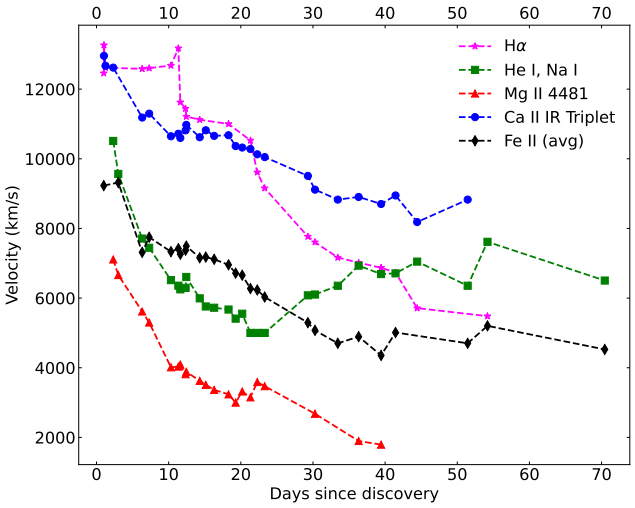

Figure 11. Evolution of line velocities for SN 2024aecx measured from Gaussian fits to the absorption minima.

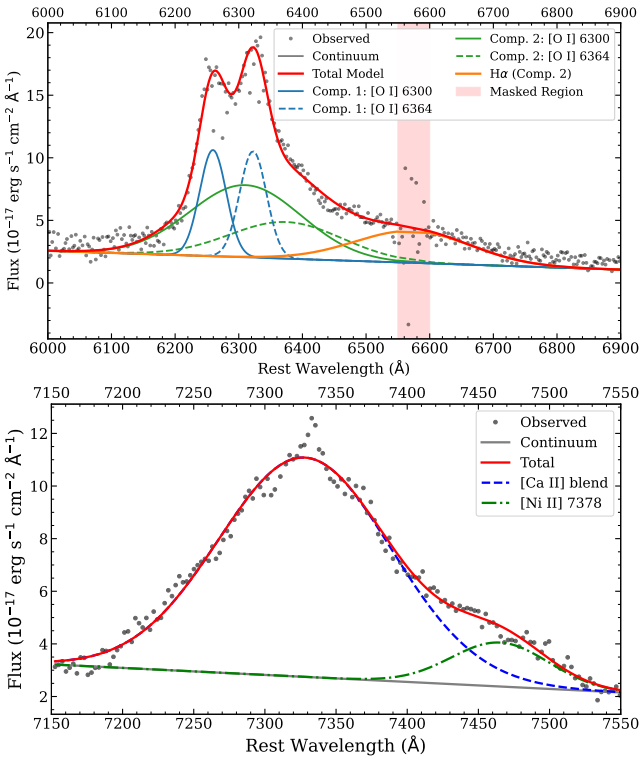

Figure 12. Multicomponent fits to nebular emission features of SN 2024aecx. Top: The [O I] $\lambda\lambda$6300, 6363 doublet modeled with two kinematic components that share $v_{\rm shift}$ and full width at half-maximum; the wavelength range affected by narrow Hα is masked (shaded band). Bottom: Simultaneous fit to the [Ca II] $\lambda\lambda$7291, 7324 blend and [Ni II] λ7378. Black points show the data, the thin gray curve the pseudocontinuum, the red curve the total model, and the colored dashed/dotted curves the individual components as indicated in the legends. Best-fit parameters are listed in Table 3.

In addition, we identify a distinct, high-velocity, blueshifted component (hereafter Component 1) exclusively in the [O I] lines. We interpret this feature as a discrete clump or knot of nearly pure oxygen-rich material ejected with a significant line-of-sight velocity component toward the observer. Its large blueshift indicates its high velocity, while its comparatively narrow FWHM suggests a small internal velocity dispersion, consistent with the kinematic signature of a coherent, localized structure. Such high-velocity features, often interpreted as compelling evidence for large-scale ejecta asymmetries, have been observed in the nebular spectra of other CCSNe, a notable example being SN 2023ixf (A. Kumar et al. 2025; P. D. Michel et al. 2025).

The flux ratio of the [O I] $\lambda\lambda$6300, 6363 doublet to the [Ca II] $\lambda\lambda$7291, 7324 doublet is regarded as a potential diagnostic of the progenitor mass for SESNe. The underlying principle is that the bulk of the oxygen is synthesized during pre-SN hydrostatic burning phases, the yield of which is highly dependent on the progenitor's initial mass. In contrast, calcium

Table 3
Emission-line fit Parameters for the Nebular Phase Spectrum of SN 2024aecx

Line	v_{shift} (km s^{-1})	FWHM (km s^{-1})	Flux (10^{-17})[a]
[O I] 6300 Comp. 1	−1945.23 ± 24.85	2354.82 ± 55.77	444.49 ± 20.94
[O I] 6363 Comp. 1	−1945.23 ± 24.85	2354.82 ± 55.77	448.97 ± 23.46
[O I] 6300 Comp. 2	475.84 ± 234.36	9770.33 ± 268.43	1262.87 ± 133.31
[O I] 6363 Comp. 2	475.84 ± 234.36	9770.33 ± 268.43	647.37 ± 114.30
[Ca II] blend	829.99 ± 31.20	5845.00 ± 106.17	1267.70 ± 30.26
[Ni II] 7378	3548.21 ± 133.57	3274.20 ± 11.76	144.93 ± 11.06

Notes. For each transition we list the velocity shift v_{shift}, the full width at half-maximum, and the integrated flux. The [O I] $\lambda\lambda$6300, 6363 doublet is fitted simultaneously with two kinematic components that share v_{shift} and full width at half-maximum; [Ca II] refers to the $\lambda\lambda$7291, 7324 blend; [Ni II] λ7378 is modeled as a single component. The corresponding spectral fit is shown in Figure 12.
[a] Flux units in erg s^{-1} cm^{-2}.

Table 4
Key Model Parameters and Priors for SN 2024aecx

Parameter	Definition	Units	Default Prior	SN 2024aecx
M_e	Extended H-rich envelope mass	$M_\odot$	$L[10^{-3}, 0.5]$	0.04 ± 0.01
R_e	Extended envelope radius	$R_\odot$	$L[10, 10^4]$	$66.75^{+25.47}_{-25.93}$
E_e	Energy of extended envelope	10^{49} erg	$L[0.01, 20]$	$0.96^{+0.97}_{-0.36}$
M_{ej}	Ejecta mass	$M_\odot$	$L[0.3, 10]$	$1.55^{+0.18}_{-0.14}$
M_{Ni}	Synthesized ^{56}Ni mass	$M_\odot$	$L[0.01, 0.3]$	0.09 ± 0.01
t_0	Explosion epoch[a]	day	$U[0, 5]$	$0.02^{+0.02}_{-0.01}$

Notes. L = log-uniform prior; U = uniform prior. The *Default Prior* column lists the priors adopted in our MCMC analysis of the bolometric light curve.
[a] Defined as the time offset between the explosion epoch and the discovery date.

is predominantly produced during explosive silicon burning, and its synthesized mass is predicted to be relatively insensitive to the progenitor mass over a wide range. Consequently, a higher [O I]/[Ca II] flux ratio is expected to correspond to a more massive progenitor (A. Jerkstrand 2017). For this SN, we measure a ratio of 2.21 ± 0.15. A comparison with the grid of nebular-phase spectral models from A. Jerkstrand et al. (2015) places our measurement between their 13 $M_\odot$ and 17 $M_\odot$ progenitor models (referred to as m13 and m17, respectively). This result is consistent with a progenitor of moderate mass, which for a SESN likely implies origin in a binary system. However, it is important to note that the utility of the [O I]/[Ca II] ratio as a robust mass indicator has been contested. Some studies have found, for instance, a weak or nonexistent correlation between this ratio and the total ejecta mass derived from light-curve modeling, casting doubt on its direct correspondence with the progenitor's zero-age main-sequence mass (e.g., S. J. Prentice et al. 2022).

6. Modeling of the Progenitor and Explosion Parameters

The evolution of a SN light curve in the hours and days immediately following the explosion is a powerful diagnostic of the progenitor star's structure and recent mass-loss history. SN 2024aecx is a compelling example, discovered shortly after its explosion, with an optical light curve that exhibits a prominent double-peaked morphology (Section 4; Figure 7). This structure is characteristic of an initial, rapidly fading peak from shock-cooling emission from an extended stellar envelope, followed by a broader, slower peak powered by the radioactive decay of ^{56}Ni and ^{56}Co. Such double-peaked light curves, famously observed in SNe such as SN 1993J and SN 2011dh, are often interpreted as evidence for progenitors with extended, low-mass hydrogen envelopes (e.g., I. Arcavi et al. 2011; M. C. Bersten et al. 2012). A statistical study based on ATLAS further indicates that nearly half of Type IIb SNe exhibit this kind of early double-peaked behavior, implying that such progenitor configurations may be relatively common within this class (B. Ayala et al. 2025).

To interpret these features in SN 2024aecx, we model its bolometric light curve using a semianalytic framework that incorporates two distinct physical components. First, the early peak is attributed to shock-cooling emission, which we calculate using the analytic prescriptions of A. L. Piro et al. (2021) to connect the peak's luminosity and duration to the envelope's mass and radius. Second, the main peak is powered by radioactive heating, which is modeled with the classical diffusion formalism of W. D. Arnett (1982) to treat the thermalization of energy from the ^{56}Ni→^{56}Co→^{56}Fe decay chain. This two-component framework provides a computationally efficient yet physically grounded description of the light curve, enabling a direct connection between its observed evolution and the underlying properties of the progenitor and explosion.

To quantitatively constrain the physical parameters governing the light curve of SN 2024aecx, we performed a comprehensive Bayesian analysis using a Markov Chain Monte Carlo (MCMC) approach. The model's parameters, their corresponding prior distributions, and the resulting best-fit values are summarized in Table 4. The fit to the bolometric light curve is presented in Figure 13. The resulting posterior probability distributions for the key physical parameters of our model are presented in the corner plot in Figure 14. As an external spectroscopic constraint, Fe II absorption features

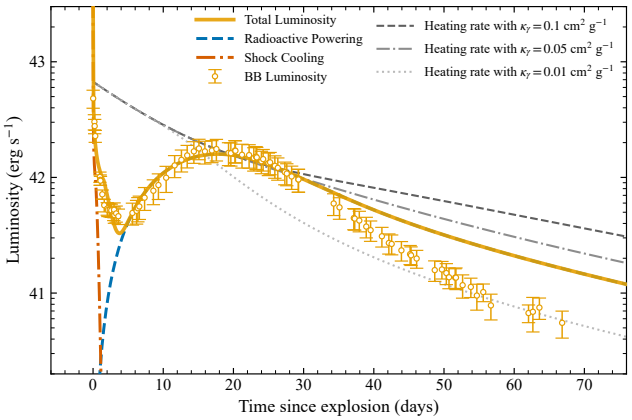

Figure 13. Bolometric light curve of SN 2024aecx (orange circles) compared with the best-fit two-component model. The solid orange curve shows the total luminosity, decomposed into radioactive powering emission (blue dashed line) and shock-cooling emission (brown dashed–dotted line). The gray curves show the instantaneous radioactive heating rate for different assumed γ-ray opacities, $\kappa_\gamma = 0.1$ (dark gray dashed), 0.05 (medium gray dashed–dotted), and 0.01 cm^2 g^{-1} (light gray dotted). The model reproduces both the early cooling peak and the main radioactive peak, while the late-time decline is steeper than the corresponding heating rate.

around maximum light indicate a photospheric velocity of $\sim$6500 km s^{-1} (Section 5; Figure 11); accordingly, we adopt $v_{\rm ej} = 6500$ km s^{-1} in the fit.

Our analysis yields an extended envelope mass of $M_{\rm e} = 0.04 \pm 0.01\,M_\odot$, radius $R_{\rm e} = 66.75^{+25.47}_{-25.93}\,R_\odot$, and characteristic energy $E_{\rm e} = 0.96^{+0.97}_{-0.36} \times 10^{49}$ erg for the shock-cooling component. For the radioactive component, we infer an ejecta mass of $M_{\rm ej} = 1.55^{+0.18}_{-0.14}\,M_\odot$, and a synthesized nickel mass of $M_{\rm Ni} = 0.09 \pm 0.01\,M_\odot$. These values are consistent with a moderately extended, low-mass hydrogen envelope and a highly energetic core-collapse explosion. These properties closely match expectations for a binary-stripped progenitor, where Roche-lobe overflow removes most of the hydrogen envelope. Indeed, all directly detected IIb progenitors to date are linked to binaries, and our results provide further support for this scenario (J. R. Maund et al. 2004; Z. Niu et al. 2024, 2025).

As shown in Figure 13, the bolometric light curve of SN 2024aecx is well reproduced by our two-component model: at very early times ($t \lesssim 5$ days) the luminosity clearly exceeds the radioactive heating curves, confirming that the first peak is dominated by shock cooling of the extended envelope rather than by ^{56}Ni decay. Around the main maximum ($\sim$10–30 days), the total luminosity is matched when adopting a γ-ray opacity of $\kappa_\gamma \simeq 0.05$ cm^2 g^{-1}, indicating efficient γ-ray trapping in the bulk of the ejecta. At later epochs ($t \gtrsim 40$ days), however, the observed luminosity declines more rapidly than predicted by the radioactive heating model, even after including the effect of γ-ray leakage from the ejecta (A. Clocchiatti & J. C. Wheeler 1997; K. Maeda et al. 2003). This suggests that the emission is no longer fully controlled by the instantaneous ^{56}Co decay power and that additional processes—such as early dust formation (C. Gall et al. 2011), incomplete positron trapping (P. A. Milne et al. 2001), or asymmetric ejecta that enhance high-energy photon escape (K. Maeda et al. 2008)—may contribute to the steep decline. Such behavior is consistent with the relatively low ejecta mass inferred from our modeling and with the rapid postpeak evolution commonly seen in SNe IIb. Even in comparison with such SESNe (e.g., SN 2008ax, S. Taubenberger et al. 2011, and SN 2011ei, D. Milisavljevic et al. 2013; see also K. Maeda et al. 2008), SN 2024aecx still declines unusually fast (Figure 8); a similar trend has been reported by X. Zou et al. (2026), suggesting that γ-ray leakage alone may not fully explain this phenomenon.

Given the derived parameters, SN 2024aecx likely originated from a progenitor with a moderately extended, low-mass hydrogen envelope and an energetic core-collapse explosion. Future multiwavelength follow-up, especially in the infrared and polarimetric domains, will be essential to test the dust-formation and ejecta-asymmetry scenarios.

In comparison with the results of X. Zou et al. (2026), our analysis of SN 2024aecx yields broadly consistent extinction estimates and a similar velocity evolution of spectral features. However, our dataset benefits from a denser spectroscopic cadence, the inclusion of nebular-phase spectra, and more extensive multiband photometry. Our modeling recovers the same ^{56}Ni mass $M_{\rm Ni} \simeq 0.09\,M_\odot$, while constraining the envelope mass to $M_{\rm e} = 0.04 \pm 0.01\,M_\odot$, which falls within the range of $\sim$0.03–0.24 $M_\odot$ reported by X. Zou et al. (2026), but with significantly tighter uncertainties and a smaller inferred envelope radius. We also derive a larger ejecta mass of $M_{\rm ej} = 1.55^{+0.18}_{-0.14}\,M_\odot$, compared to the $\sim$0.7 $M_\odot$ obtained by X. Zou et al. (2026). Further detailed investigations of the photometric and spectroscopic evolution of this SN are warranted.

7. Summary

We presented a comprehensive UV–optical study of the Type IIb SN 2024aecx in NGC 3521. SN 2024aecx was discovered within $\sim$1 day from the last nondetections, and our follow-up campaign started from as early as $t = 0.26$ day after discovery and continued out to the nebular phase.

With the TRGB method, we obtain a new distance of $D = 11.3 \pm 1.1$ Mpc to the host galaxy. VLT/MUSE spectroscopy of the cospatial H II region indicates a near-solar abundance of $12 + \log({\rm O/H}) = 8.49 \pm 0.18$ (O3N2). We also derive a host extinction of $A_V^{\rm Host} \simeq 1.2$ mag toward SN 2024aecx.

The light curves display a short-lived early peak, attributable to the cooling of a shock-heated extended surface layer, followed by a secondary maximum and an unusually rapid postpeak decline. While the peak luminosity falls within the typical range for this SN class, both the shock-cooling phase and the subsequent decline after the secondary maximum proceed at an exceptionally fast pace.

The earliest spectra at $t = 0.3$–1.2 days display a blue, nearly featureless continuum. From $t = 2.3$ days, P-Cygni features emerge and we derived the velocity evolution of Hα, He I λ5876, Mg II λ4481, the Ca II infrared triplet, and the Fe II triplet. We took three nebular-phase spectra at $t = 71.5$, 123.5, 158.5 days. The [O I] and [Ca II] lines exhibit asymmetric, double-peaked profiles, which may arise from asphericity and/or early dust formation.

Our modeling of the nebular-phase spectrum of SN 2024aecx reveals a highly asymmetric explosion geometry. The observed line profiles can be well reproduced by a model consisting of a prominent, blueshifted oxygen-rich clump of ejecta, superimposed on a slightly redshifted bulk component. We measure the flux ratio of the [O I] $\lambda\lambda$6300, 6364 doublet to the [Ca II] $\lambda\lambda$7291, 7324 doublet to be approximately 2. This value

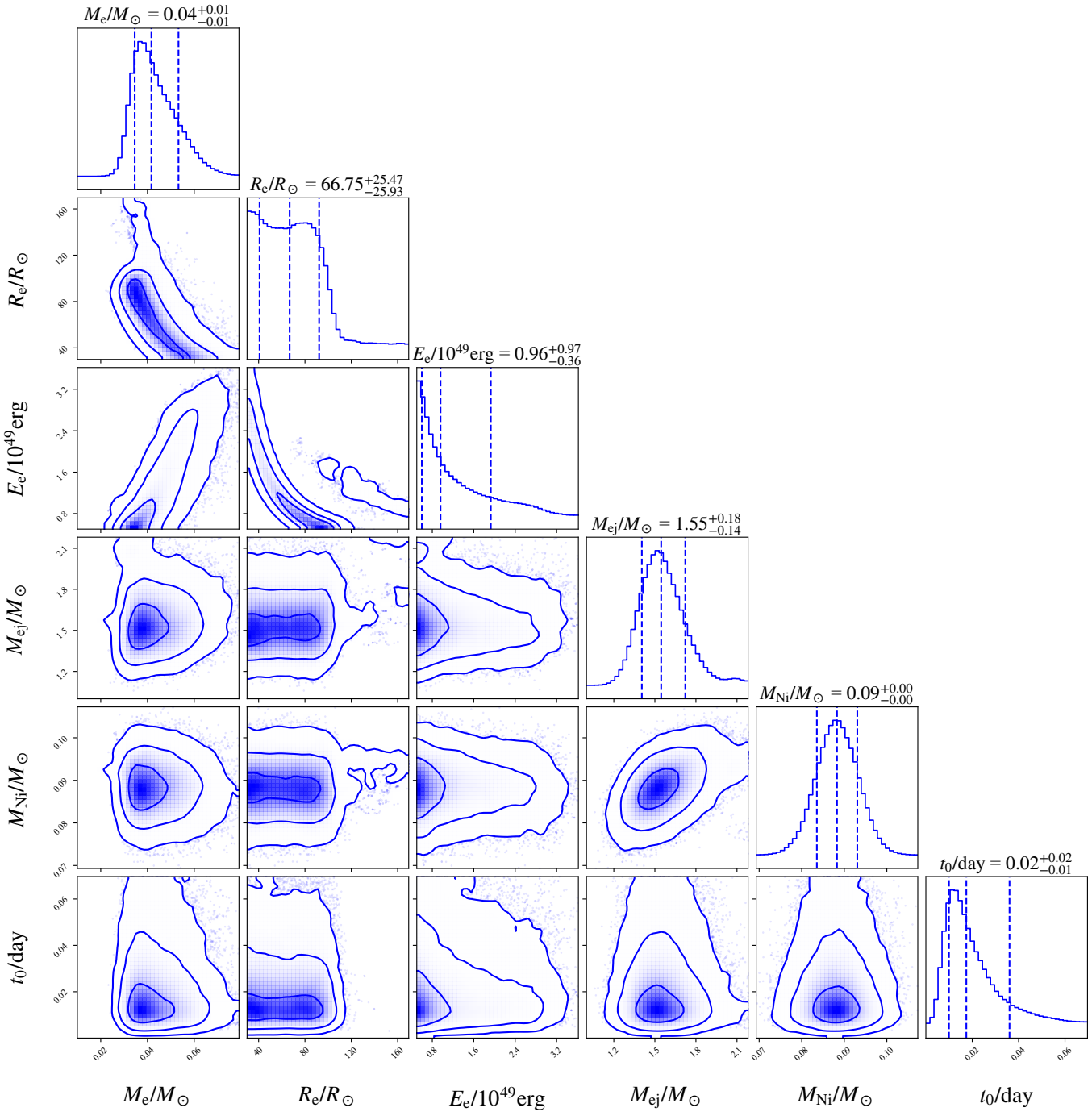

Figure 14. The posterior probability distributions and covariances for the key physical parameters of SN 2024aecx from our MCMC analysis.

is consistent with those observed in other CCSNe, suggesting that SN 2024aecx likely arose from a progenitor of moderate mass, possibly in a binary system.

A two-component model combining shock cooling and ^{56}Ni heating reproduces the overall double-peaked morphology of the bolometric light curve. Inference favors a dilute, extended H-rich envelope ($M_e = 0.04 \pm 0.01\,M_\odot$, $R_e = 66.75^{+25.47}_{-25.93}\,R_\odot$) and a SESNe explosion with an ejecta mass of $M_{ej} = 1.55^{+0.18}_{-0.14}\,M_\odot$ and $M_{Ni} = 0.09 \pm 0.01\,M_\odot$. The late-time decline proceeds faster than expected, suggesting enhanced γ-ray leakage and/or dust formation. The nebular-phase spectra and light-curve modeling both suggest that it most likely originated from an intermediate-mass binary progenitor system.

SN 2024aecx is one of the well-sampled Type IIb SNe: at a very close distance, discovered at an exceptionally early phase, and exhibiting one of the most prominent shock-cooling flashes among Type IIb SNe. The combination of high-cadence photometric and spectroscopic follow-up observations along with the well-characterized environment provides stringent constraints on the progenitor and its explosion. The data and analysis presented here offer a high-quality reference for shock-cooling physics and progenitor-envelope coupling in Type IIb SNe. Future NIR photometry and mid-IR spectroscopy can directly test dust formation, radio/X-ray observations will probe circumstellar interaction and recent mass loss, and

nebular radiative-transfer modeling and spectropolarimetry will further quantify ejecta geometry.

Acknowledgments

We are grateful to Prof. Luc Dessart and Prof. Anders Jerkstrand for their valuable discussions and suggestions regarding the nebular-phase spectra. We also thank Prof. Nancy Elias-Rosa for her helpful discussions during the course of this work. We thank the anonymous referee for the time devoted to reviewing our manuscript and for the valuable comments.

N.C.S. is funded by the Strategic Priority Research Program of the Chinese Academy of Sciences grant No. XDB0550300, the National Natural Science Foundation of China grants Nos. 12303051 and 12261141690, and the China Manned Space Program No. CMS-CSST-2025-A14. F.P. acknowledges support from the Spanish Ministerio de Ciencia, Innovación y Universidades (MICINN) under grant numbers PID2022-141915NB-C21. K.M., B.A., and D.K. acknowledge the support from the BRICS grant DST/ICD/BRICS/Call-5/CoNMuTraMO/2023 (G) funded by the Department of Science and Technology (DST), India. L.L. and Y.Z. acknowledge the support from the National Natural Science Foundation of China (grant Nos 12303047) and Natural Science Foundation of Hubei Province (2023AFB321).

Z.G. acknowledges the support supported from the China-Chile Joint Research Fund (CCJRF No. 2301) and the Chinese Academy of Sciences South America Center for Astronomy (CASSACA) Key Research Project E52H540301. Z.G., is funded by ANID, Millennium Science Initiative, AIM23-001. W.X.L. acknowledges the support from National Key R&D Program of China (grant Nos. 2023YFA1607804, 2022YFA1602902, 2023YFA1607800, and 2023YFA1608100), the National Natural Science Foundation of China (grant Nos. 12120101003, 12373010, 12173051, and 12233008), China Manned Space Project (No. CMS-CSST-2025-A06), and the Strategic Priority Research Program of the Chinese Academy of Sciences with grant Nos. XDB0550100 and XDB0550000. L.Z.W. is sponsored by the National Natural Science Foundation of China (NSFC) grant No. 12573050, the Chinese Academy of Sciences South America Center for Astronomy (CASSACA) Key Research Project E52H540301, and in part by the Chinese Academy of Sciences (CAS) through a grant to the CASSACA. J.D.L. acknowledges support from a UK Research and Innovation Future Leaders Fellowship (MR/T020784/1). B.C.W. acknowledges support from the National Key R&D Program of China (grant Nos. 2023YFA1609700, 2023YFA1608304), the National Natural Science Foundation of China (NSFC; grant Nos. 12090040, 12090041, 12403022), and the Strategic Priority Research Program of the Chinese Academy of Sciences (grant Nos. XDB0550000, XDB0550100, XDB0550102).

Based on observations made with the Thai Robotic Telescopes (TRT) under program IDs TRTC12A_003, TRTC12A_002, TRTToO_2024006, and TRTC11C_007, operated by the National Astronomical Research Institute of Thailand (Public Organization).

We thank the staff at all participating observatories, including the Xinglong 60 cm (XL-60) and 2.16 m(XL-216) telescopes, the 70 cm telescope of the University of Chinese Academy of Sciences (UCAS-70) telescope, the Devasthal Fast Optical Telescope (DFOT), the Liverpool Telescope (LT), the TRT network, the Las Cumbres Observatory Global Telescope network (LCO), the Himalayan Chandra Telescope (HCT), the Devasthal Optical Telescope (DOT), the Nordic Optical Telescope (NOT), and the Gran Telescopio Canarias (GTC), for their support during our observing campaigns.

We acknowledge the use of data and services provided by ATLAS, ZTF, GOTO, Swift/UVOT, the Transient Name Server (TNS), the Mikulski Archive for Space Telescopes (MAST), and the ESO Science Archive Facility. This research has made use of NASA's Astrophysics Data System (ADS). We also acknowledge the use of open-source software packages, including ASTROPY, AUTOPHOT, HOTPANTS, IRAF, and PYPEIT.

Facilities: ARIES:DFOT, ARIES:DOT, GTC, HCT, HST/ACS, Liverpool:2m (LT), NOT, Swift/UVOT, TRT, UCASST, VLT:Yepun (MUSE), Beijing:0.6m (XL-60), Beijing:1.26m (XL-216).

Software: astropy (Astropy Collaboration et al. 2013, 2018, 2022), AutoPhot (S. J. Brennan & M. Fraser 2024), hotpants (A. Becker 2015), IRAF (D. Tody 1986), PypeIt (J. Prochaska et al. 2020).

ORCID iDs

Ning-Chen Sun https://orcid.org/0000-0002-4731-9698
David Aguado https://orcid.org/0000-0001-5200-3973
Frédérick Poidevin https://orcid.org/0000-0002-5391-5568
Junjie Jin https://orcid.org/0000-0002-8402-3722
Zexi Niu https://orcid.org/0000-0002-3651-0681
Kuntal Misra https://orcid.org/0000-0003-1637-267X
Justyn R. Maund https://orcid.org/0000-0003-0733-7215
Amit Kumar https://orcid.org/0000-0002-4870-9436
Samaporn Tinyanont https://orcid.org/0000-0002-1481-4676
Liang-Duan Liu https://orcid.org/0000-0002-8708-0597
Monalisa Dubey https://orcid.org/0009-0002-2621-6611
Zhen Guo https://orcid.org/0000-0003-0292-4832
Min He https://orcid.org/0000-0001-6139-7660
Dhruv Jain https://orcid.org/0009-0004-7242-4301
Joe D. Lyman https://orcid.org/0000-0002-3464-0642
Xinxiang Sun https://orcid.org/0009-0002-0735-3274
Lingzhi Wang https://orcid.org/0000-0002-1094-3817
Yi-Han Zhao https://orcid.org/0009-0005-9841-1434
Jie Zheng https://orcid.org/0000-0001-6637-6973
Alicia López Oramas https://orcid.org/0000-0003-4603-1884
Yanan Wang https://orcid.org/0000-0003-3207-5237
Klaas Wiersema https://orcid.org/0000-0002-9133-7957
Jifeng Liu https://orcid.org/0000-0002-2874-2706

References

Ahn, C. P., Alexandroff, R., Allende Prieto, C., et al. 2014, ApJS, 211, 17
Anand, G., Lee, J., van Dyk, S., et al. 2020, AAS Meeting, 236, 336.01
Andrews, J., Bostroem, K. A., Sand, D. J., et al. 2024a, TNSCR, 2024-4974, 1
Andrews, J., Sand, D. J., Bostroem, K. A., et al. 2024b, TNSCR, 2024-4943, 1
Arcavi, I., Kasliwal, M. M., Quimby, R. M., et al. 2011, ApJL, 742, L18
Arnett, W. D. 1982, ApJ, 253, 785
Asplund, M., Grevesse, N., Sauval, A. J., & Scott, P. 2009, ARA&A, 47, 481
Astropy Collaboration, Price-Whelan, A. M., Lim, P. L., et al. 2022, ApJ, 935, 167
Astropy Collaboration, Price-Whelan, A. M., Sipőcz, B. M., et al. 2018, AJ, 156, 123
Astropy Collaboration, Robitaille, T. P., Tollerud, E. J., et al. 2013, A&A, 558, A33
Ayala, B., Anderson, J. P., Pignata, G., et al. 2025, A&A, 701, A128
Baade, W. 1944, ApJ, 100, 137

Bacon, R., Accardo, M., Adjali, L., et al. 2010, SPIE, 7735, 773508
Becker, A., 2015 HOTPANTS: High Order Transform of PSF ANd Template Subtraction, Astrophysics Source Code Library, ascl:1504.004
Bersten, M. C., Benvenuto, O. G., Nomoto, K., et al. 2012, ApJ, 757, 31
Bevan, A., & Barlow, M. J. 2016, MNRAS, 456, 1269
Brennan, S. J., & Fraser, M., 2024 AutoPhOT: Rapid Publication-quality Photometry of Transients, Astrophysics Source Code Library, ascl:2406.030
Brown, T. M., Baliber, N., Bianco, F. B., et al. 2013, PASP, 125, 1031
Bruzual, G., & Charlot, S. 2003, MNRAS, 344, 1000
Cardelli, J. A., Clayton, G. C., & Mathis, J. S. 1989, ApJ, 345, 245
Cepa, J., Aguiar, M., Escalera, V. G., et al. 2000, SPIE, 4008, 623
Cid Fernandes, R., Mateus, A., Sodré, L., Stasińska, G., & Gomes, J. M. 2005, MNRAS, 358, 363
Clocchiatti, A., & Wheeler, J. C. 1997, ApJ, 491, 375
Cowsik, R., Srinivasan, R., & Prabhu, T. P. 2002, BASI, 30, 105
Da Costa, G. S., & Armandroff, T. E. 1990, AJ, 100, 162
Dessart, L., Hillier, D. J., Woosley, S., et al. 2015, MNRAS, 453, 2189
Djupvik, A. A., & Andersen, J. 2010, in Highlights of Spanish Astrophysics V: Astrophysics and Space Science Proceedings, 14, ed. J. M. Diego et al. (Springer), 211
Dolphin, A., 2016 DOLPHOT: Stellar photometry, Astrophysics Source Code Library, ascl:1608.013
Edmunds, M. G., & Pagel, B. E. J. 1984, MNRAS, 211, 507
Ergon, M., Sollerman, J., Fraser, M., et al. 2014, A&A, 562, A17
Fan, Z., Wang, H., Jiang, X., et al. 2016, PASP, 128, 115005
Fang, Q., Maeda, K., Kuncarayakti, H., et al. 2022, ApJ, 928, 151
Fang, Q., Maeda, K., Kuncarayakti, H., & Nagao, T. 2024, NatAs, 8, 111
Fang, Q., Maeda, K., Kuncarayakti, H., Sun, F., & Gal–Yam, A. 2019, NatAs, 3, 434
Filippenko, A. V. 1988, AJ, 96, 1941
Filippenko, A. V. 1997, ARA&A, 35, 309
Gall, C., Hjorth, J., & Andersen, A. C. 2011, A&ARv, 19, 43
Gehrels, N., Chincarini, G., Giommi, P., et al. 2004, ApJ, 611, 1005
Henden, A. A., Levine, S., Terrell, D., & Welch, D. L. 2015, AAS Meeting, 225, 336.16
Hinkle, J. 2024, TNSC R, 2024-4947, 1
Jerkstrand, A. 2017, in Handbook of Supernovae, ed. A. W. Alsabti & P. Murdin (Springer), 795
Jerkstrand, A., Ergon, M., Smartt, S. J., et al. 2015, A&A, 573, A12
Jester, S., Schneider, D. P., Richards, G. T., et al. 2005, AJ, 130, 873
Joshi, Y. C., Bangia, T., Jaiswar, M. K., et al. 2022, JAI, 11, 2240004
Kumar, A., Dastidar, R., Maund, J. R., Singleton, A. J., & Sun, N.-C. 2025, MNRAS, 538, 659
Kumar, B., Pandey, S. B., Sahu, D. K., et al. 2013, MNRAS, 431, 308
Langer, N. 2012, ARA&A, 50, 107
Lee, M. G., Freedman, W. L., & Madore, B. F. 1993, ApJ, 417, 553
Lyman, J. D., Bersier, D., James, P. A., et al. 2016, MNRAS, 457, 328
Lyman, J. D., Taddia, F., Stritzinger, M. D., et al. 2018, MNRAS, 473, 1359
Maeda, K., Kawabata, K., Mazzali, P. A., et al. 2008, Sci, 319, 1220
Maeda, K., Mazzali, P. A., Deng, J., et al. 2003, ApJ, 593, 931
Mao, Y., Ge, L., Sun, Y., et al. 2025, AstTI, 2, 198
Marino, R. A., Rosales-Ortega, F. F., Sánchez, S. F., et al. 2013, A&A, 559, A114
Maund, J. R., Smartt, S. J., Kudritzki, R. P., Podsiadlowski, P., & Gilmore, G. F. 2004, Natur, 427, 129
Michel, P. D., Mazzali, P. A., Perley, D. A., Hinds, K.-R., & Wise, J. L. 2025, MNRAS, 539, 633
Milisavljevic, D., Margutti, R., Soderberg, A. M., Fesen, R. A., et al. 2013, ApJ, 767, 71
Milne, P. A., The, L.-S., & Leising, M. D. 2001, ApJ, 559, 1019
Minkowski, R. 1941, PASP, 53, 224
Morales-Garoffolo, A., Elias-Rosa, N., Benetti, S., et al. 2014, MNRAS, 445, 1647
Morales-Garoffolo, A., Elias-Rosa, N., Bersten, M., et al. 2015, MNRAS, 454, 95
Mu, H.-Y., Fan, Z., Zhu, Y.-N., Zhang, Y., & Wu, H. 2024, RAA, 24, 055009
Nicholl, M. 2018, RNAAS, 2, 230
Niu, Z., Sun, N.-C., & Liu, J. 2024, ApJL, 970, L9
Niu, Z., Sun, N.-C., Maund, J. R., et al. 2025, ApJL, 987, L10
Osterbrock, D. E., & Ferland, G. J. 2006, Astrophysics of Gaseous Nebulae and Active Galactic Nuclei (Univ. Science Books)
Pagel, B. E. J., Edmunds, M. G., Blackwell, D. E., Chun, M. S., & Smith, G. 1979, MNRAS, 189, 95
Pandey, S. B., Kumar, A., Kumar, B., et al. 2021, MNRAS, 507, 1229
Pérez-Fournon, I., Aguado, D. S., Poidevin, F., et al. 2024, TNSAN, 374, 1
Piro, A. L., Haynie, A., & Yao, Y. 2021, ApJ, 909, 209
Poznanski, D., Prochaska, J. X., & Bloom, J. S. 2012, MNRAS, 426, 1465
Prabhu, T. P. 2014, PINSA, 80, 887
Prentice, S. J., Maguire, K., Siebenaler, L., & Jerkstrand, A. 2022, MNRAS, 514, 5686
Prochaska, J., Hennawi, J., Westfall, K., et al. 2020, JOSS, 5, 2308
Rizzi, L., Tully, R. B., Makarov, D., et al. 2007, ApJ, 661, 815
Rodríguez, Ó., Maoz, D., & Nakar, E. 2023, ApJ, 955, 71
Roming, P. W. A., Kennedy, T. E., Mason, K. O., et al. 2005, SSRv, 120, 95
Sagar, R., Kumar, B., & Sharma, S. 2020, JApA, 41, 33
Sandage, A. 1971, ApJ, 166, 13
Savitzky, A., & Golay, M. J. E. 1964, AnaCh, 36, 1627
Schlegel, D. J., Finkbeiner, D. P., & Davis, M. 1998, ApJ, 500, 525
Schmidt, B. P., Kirshner, R. P., Eastman, R. G., et al. 1993, Natur, 364, 600
Smartt, S. J. 2009, ARA&A, 47, 63
Smith, N. 2014, ARA&A, 52, 487
Steeghs, D., Galloway, D. K., Ackley, K., et al. 2022, MNRAS, 511, 2405
Steele, I. A. 2001, AN, 322, 307
Stevance, H., Smith, K. W., Young, D. R., et al. 2024, TNSAN, 371, 1
Stritzinger, M. D., Taddia, F., Burns, C. R., et al. 2018, A&A, 609, A135
Subrayan, B. M., Sand, D. J., Bostroem, K. A., et al. 2025, ApJL, 990, L68
Sun, N.-C., Maund, J. R., & Crowther, P. A. 2023a, MNRAS, 521, 2860
Sun, N.-C., Maund, J. R., Crowther, P. A., Fang, X., & Zapartas, E. 2021, MNRAS, 504, 2253
Sun, N.-C., Maund, J. R., Crowther, P. A., et al. 2022, MNRAS, 510, 3701
Sun, N.-C., Maund, J. R., Shao, Y., & Janiak, I. A. 2023b, MNRAS, 519, 3785
Taddia, F., Stritzinger, M. D., Bersten, M., et al. 2018, A&A, 609, A136
Tartaglia, L., Fraser, M., Sand, D. J., et al. 2017, ApJL, 836, L12
Taubenberger, S., Navasardyan, H., Maurer, J. I., et al. 2011, MNRAS, 413, 2140
Taubenberger, S., Valenti, S., Benetti, S., et al. 2009, MNRAS, 397, 677
Tody, D. 1986, SPIE, 627, 733
Tucker, M. A., Shappee, B. J., Huber, M. E., et al. 2022, PASP, 134, 124502
Turatto, M., Benetti, S., & Cappellaro, E. 2003, in From Twilight to Highlight: The Physics of Supernovae, ed. W. Hillebrandt & B. Leibundgut (Springer), 200
Woosley, S. E., & Heger, A. 2007, PhR, 442, 269
Xi, Q., Sun, N.-C., Zhao, Y.-H., et al. 2025, MNRAS, 542, 1852
Yoon, S. C., Woosley, S. E., & Langer, N. 2010, ApJ, 725, 940
Zou, X., Kumar, B., Singh Teja, R., et al. 2026, ApJ, 997, 77